Significant Impact of Hydrothermalism on the Biogeochemical Signature of Sinking and Sedimented Particles in the Lau Basin

Chloé Tilliette, Frédéric Gazeau, Valérie Chavagnac, Nathalie Leblond, Maryline Montanes, Karine Leblanc, Sabine Schmidt, Bruno Charrière, Nagib Bhairy, Cécile Guieu

JGR Oceans

RESEARCH ARTICLE
10.1029/2023JC019828

Key Points:

- Lithogenic material of hydrothermal origin drives the biological production of the Lau Basin
- Hydrothermal sources impact the biogeochemical signature of particles on large spatio-temporal scales
- The Late'iki volcanic eruption had an impact on the deep layer of the entire Lau Basin

Supporting Information:

Supporting Information may be found in the online version of this article.

Correspondence to:

C. Tilliette and C. Guieu,
chloe.tilliette@imev-mer.fr;
cecile.guieu@imev-mer.fr

Citation:

Tilliette, C., Gazeau, F., Chavagnac, V., Leblond, N., Montanes, M., Leblanc, K., et al. (2023). Significant impact of hydrothermalism on the biogeochemical signature of sinking and sedimented particles in the Lau Basin. *Journal of Geophysical Research: Oceans*, *128*, e2023JC019828. https://doi.org/10.1029/2023JC019828

Received 13 MAR 2023
Accepted 2 NOV 2023

Significant Impact of Hydrothermalism on the Biogeochemical Signature of Sinking and Sedimented Particles in the Lau Basin

Chloé Tilliette[1], Frédéric Gazeau[1], Valérie Chavagnac[2], Nathalie Leblond[1], Maryline Montanes[1], Karine Leblanc[3], Sabine Schmidt[4], Bruno Charrière[5], Nagib Bhairy[3], and Cécile Guieu[1]

[1]Laboratoire d'Océanographie de Villefranche, Sorbonne Université, CNRS, Villefranche-sur-Mer, France, [2]Géosciences Environnement Toulouse, CNRS, Université de Toulouse, IRD, Toulouse, France, [3]Aix Marseille University, Université de Toulon, CNRS, IRD, Marseille, France, [4]University Bordeaux, CNRS, Bordeaux INP, EPOC, Pessac, France, [5]Centre de Formation et de Recherche sur l'Environnement Méditerranéen (CEFREM, UMR CNRS 5110), Bât. U, Université de Perpignan, Via Domitia (UPVD), Perpignan, France

Abstract Iron (Fe) is an essential micronutrient for diazotrophs, which are abundant in the Western Tropical South Pacific Ocean (WTSP). Their success depends on the numerous trace metals, particularly Fe, released from shallow hydrothermal vents along the Tonga Arc. This study aimed to explore the spatio-temporal impact of hydrothermal fluids on particulate trace metal concentrations and biological activity. To identify the composition of sinking particles across a wide area of the WTSP, we deployed sediment traps at various depths, both close and further west of the Tonga Arc. Seafloor sediments were cored at these deployment sites, including at a remote location in the South Pacific Gyre. The sinking particles were composed of a large amount of biological material (up to 88 mg d^{-1}), indicative of the high productivity of the region. A significant portion of this material (~21 ± 12 wt.%) was lithogenic of hydrothermal origin, as revealed through Al-Fe-Mn tracing. The sinking material showed similar patterns between lithogenic and biogenic fractions, indicating that hydrothermal input within the photic layer triggered surface production. A hydrothermal fingerprint was suggested in the sediments due to the high sedimentation rates (>47 cm kyr^{-1}) and the presence of large, heterogeneous, metal-rich particles. The presence of nearby active deep hydrothermal sources was suspected near the Lau Ridge due to the large particle size (1–976 μm) and the significant excess of Fe and Mn (2–20 wt.%). Overall, this study revealed that hydrothermal sources have a significant influence on the biogeochemical signature of particles in the region.

Plain Language Summary Iron is an essential micronutrient for phytoplankton growth, especially diazotrophs. In a certain area of the Pacific Ocean, they can obtain the iron they need from material released by hydrothermal vents along the Tonga Arc. We demonstrated how hydrothermal sources affect the amount of iron and other materials released into the water column and their influence on phytoplankton. We collected sinking particles and seafloor sediments and examined their chemical composition. The sinking material consisted of a large amount of biological material, indicative of the high productivity of the area. A large part of the particles collected were minerals from hydrothermal vents. These biological and metallic materials displayed similar export patterns, indicating the role of hydrothermal sources in driving surface ocean productivity. Seafloor sediments were also influenced by hydrothermalism, as suggested by their high metal contents, high sedimentation rates and large, heterogeneous particle size. In addition, an undiscovered hydrothermal source was potentially identified near the Lau Ridge based on these data. Overall, this study revealed the significant impact of hydrothermalism on the biogeochemical signature of the particles in the Lau Basin at large spatial and temporal scales.

1. Introduction

The Western Tropical South Pacific (WTSP) Ocean (160°E to 160°W) has been identified as a hotspot for dinitrogen (N_2) fixation by diazotroph organisms (Bonnet et al., 2017). The success of these species relies on the high, non-limiting surface concentrations (>0.3 nmol L^{-1}; Johnson et al., 1997) of iron (Fe) in the region, as Fe is a major component of the nitrogenase enzyme that catalyzes the N_2 fixation process (Raven, 1988). Recently, Tilliette et al. (2022) revealed that these high dissolved Fe (DFe) concentrations (up to 48 nmol L^{-1}) originate from shallow hydrothermal sources (<300 m) hosted along the Tonga-Kermadec Arc that fertilize the photic zone

of the entire Lau Basin with DFe, forming a productivity patch as large as 360,000 km^2 (analogous to the Caspian Sea area; Bonnet, Guieu et al., 2023).

The Tonga-Kermadec Arc is the most linear, convergent and seismically active subduction zone on Earth (Timm et al., 2013) and consequently exhibits the highest density of submarine volcanoes and associated hydrothermal sources (Massoth et al., 2007; Pelletier et al., 1998; Stoffers et al., 2006). Such systems release extensive plumes enriched in numerous chemical species relative to the overlying water column (Dick et al., 2013; González-Vega et al., 2020; Lilley et al., 2013) including gases (e.g., H_2S—hydrogen sulfide, CO_2—carbon dioxide, CH_4—methane), macronutrients and dissolved and particulate trace metals (e.g., Fe, Mn—manganese, Cu—copper, Zn—zinc, Pb—lead, Ni—nickel). In the Lau Basin, most of these plumes originate from sources located at depth (>1,000 m; Beaulieu & Szafrański, 2020; Lupton et al., 2004; Massoth et al., 2007), but shallower active sources (<500 m) have also been identified (Beaulieu & Szafrański, 2020; Guieu et al., 2018; Massoth et al., 2007). Two shallow hydrothermal sites were investigated as part of the TONGA cruise (Guieu and Bonnet, 2019), revealing an 80-fold enrichment of DFe concentrations (<0.45 μm) above the source relative to unimpacted waters of the WTSP (Tilliette et al., 2022). Despite their decrease toward the surface, elevated concentrations (0.6–10 nmol L^{-1}) persisted in the photic layer (0–150 m) allowing to sustain high rates of primary production (90–145 mmol C m^{-2} d^{-1}). Although the effects of such hydrothermal fertilization on biological activity are beginning to be elucidated on short temporal scales (Tilliette et al., 2023), its effects on the biogeochemical signature of the exported and sedimented particles on larger temporal and spatial scales remain unclear.

Sediment traps are classically used to explore biogeochemical cycles in the ocean and since pioneering studies (e.g., Deuser, 1987; Deuser and Ross, 1980; Honjo et al., 1992), these devices have shown their potential to highlight the variability of the composition and fluxes of biological material in relation to surface productivity, depth or season. On their descent, in particular in the mesopelagic zone (200–1,000 m), biological particles are subjected to intense bacterial remineralization and grazing by zooplankton (Boyd & Trull, 2007; Ducklow et al., 2001; Volk and Hoffert, 2013). Only a minor proportion of this material will eventually reach the deep-sea (>1,000 m) and an even smaller proportion will be buried in seafloor sediments (Berger et al., 1989; Hüneke and Henrich, 2011).

In this study, we determined the composition (i.e., lithogenic, organic matter, calcium carbonate—$CaCO_3$ and opal) of sinking and sedimented particles at different spatial and temporal scales over a large area of the WTSP, including two sites located along the Tonga Arc. The aim was to better understand how hydrothermal activity influences this region, both in terms of hydrothermally-derived trace metal concentrations and their influence on biological activity, and how volcanic activity impacts the footprint of metal particles. Ultimately, this study established whether hydrothermal sources have a significant influence on the biogeochemical signature of particles in the Lau Basin at large spatial (up to 200 km from the arc, over the entire water column) and temporal (from seasonal to centennial scales in seafloor sediments) scales.

2. Materials and Methods

This study was conducted as part of the TONGA cruise (GEOTRACES GPpr14; Guieu and Bonnet, 2019) onboard the R/V L'Atalante from October 31 to 5 December 2019, along a 6,100 km-long transect crossing the Lau Basin (Figure 1). Two shallow hydrothermal sources were identified at depths of 200 and 300 m, respectively (Tilliette et al., 2022). Mooring lines were deployed west of these sources (~15 km; stations 5 and 10) along the main current direction once the seafloor reached ~2,000 m.

2.1. Fieldwork

At stations 5 and 10, drifting conical sediment traps with a collection area of 1 m^2 (PPS-5, Technicap, France) were deployed at 200 and 1,000 m on a surface-tethered drifter. Settling particles were collected at 24-hr intervals for 5 days at station 5 (21°9.14' S, 175°44.42' W; November 10–14, 2019), and at 23-hr intervals for 4 days at station 10 (19°24.54' S, 175°7.34' W; November 24–27, 2019). Unfortunately, due to a malfunction of the PPS-5 plate motor, no samples were collected at 200 m at station 5. At station 12 (20°42.41' S, 177°52.13' W), two PPS-5 were deployed at 200 and 1,000 m on a fixed mooring line for 1 year (November 2019 to October 2020, sampling interval: 14 days). The fixed mooring line was equipped with two inclinometers (NKE S2IP) and two current meters (Nortek Aquadopp) placed at 222 and 1,030 m. The angles and velocities at both depths are shown in Figure S1 in Supporting Information S1. Each collection cup was filled with a 5% buffered formaldehyde

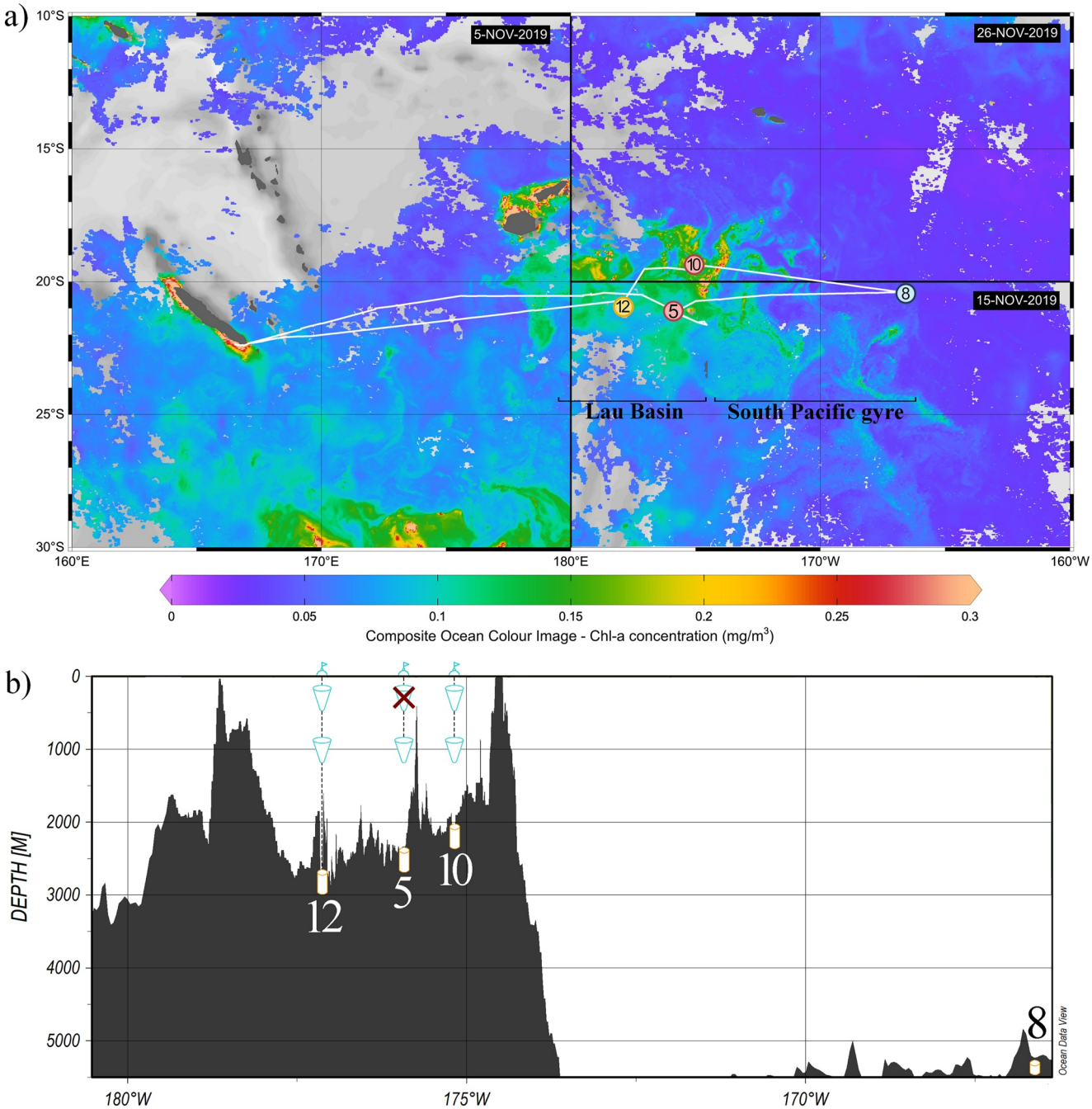

Figure 1. (a) Cruise transect superimposed on surface chlorophyll-*a* concentrations (mg m^{-3}; Bonnet, Guieu et al., 2023). Different oceanic regions were occupied during the cruise: the South Pacific gyre (station 8; sediment coring only) and the Lau Basin (stations 5 and 10), where a drifting mooring line was deployed for 5 and 4 days, respectively, as well as station 12 where a fixed mooring line was deployed for 1 year. Sediments were cored at each of these stations. Chlorophyll-*a* concentrations were derived from satellite images acquired during the respective period of occupancy: 5 November 2019 for the western part of the transect, 15 November for the southeastern part, and 29 November for the northeastern part. (b) Bathymetry along the cruise transect and instrumentation deployed at each station: sediment traps (cones) and sediment coring (cylinders).

solution prepared with filtered in-situ seawater to prevent microbial degradation and swimmer grazing. After trap recovery during the TONGA-RECUP cruise onboard the R/V Alis in December 2020 (Guieu, 2020), the cups were stored in the dark at 4°C.

Sediment cores were collected at around 10 p.m. using a MC-8/100 multi-corer (Oktopus GmbH, Kiel, Germany) at the mooring positions and at the deep-sea reference site (station 8; 20°23.33' S, 166°25.4' W; Figure 1). The

Table 1
Composition (wt.%—Percentage by Weight) and Sedimentation Rate of Seafloor Sediments at Each Station

Station	Depth	CaCO3	Opal	Organic matter	Lithogenic	Sedimentation rates
–	m			wt.%		cm kyr^{-1}
Station 5	2,140	2 ± 1	9 ± 1	0.1 ± 0.03	90 ± 1	58 ± 10
Station 10	1,930	4 ± 1	7 ± 1	0.1 ± 0.03	88 ± 3	47 ± 7
Station 12	1,940	64 ± 1	13 ± 1	0.4 ± 0.1	23 ± 3	61 ± 6
Station 8	5,326	0.3 ± 0.1	11 ± 0.1	0.6 ± 0.2	88 ± 2	58*

Note. Due to Ra enrichment of probable hydrothermal origin at station 8, the estimated sedimentation rate has been given as an indication only (see Section 3.4).

seafloor depth for each core is specified in Table 1. Immediately after collection, the first 16 cm of collected cores were divided into 1–5 cm slices, depending on the stations (see Figure 3) and frozen at −20°C.

2.2. Laboratory Work

2.2.1. Elemental Composition of Sinking Material and Seafloor Sediments

Sediment trap samples were processed by the "Cellule Pièges" (INSU-CNRS: https://www.imev-mer.fr/web/?p=526). For each sediment trap cup, swimmers were carefully removed with Teflon tweezers under a stereomicroscope (Leica Wild MZ8). Any visible material attached to the swimmers was removed whenever possible, to avoid biasing particle flux. Samples were then rinsed three times with 50 mL of MilliQ water to remove salts and lyophilized for 7 days. The total weight (wt) of each sample was measured on a Sartorius precision balance (±0.01 mg).

Seafloor sediment samples were thawed at room temperature and lyophilized for 7 days.

Both seafloor sediments and sediment trap samples were then split in different pre-weighted aliquots (~10–20 mg) for various analyses. Total carbon was measured with a CHN elemental analyzer (2400 Series II CHNS/O, Perkin Elmer®; precision ± 0.3%). Particulate organic carbon (POC) was determined similarly, after particulate inorganic carbon (PIC) removal by acidification with 2 N hydrochloric acid. Biogenic (BSi) and lithogenic (LSi) silica measurements were performed after sodium hydroxide (NaOH) and hydrofluoric acid (HF) digestion following the exact protocol described by Mosseri et al. (2005) and adapted from Brzezinski and Nelson (1995). For each aliquot, BSi was initially dissolved by NaOH digestion at 95°C for 5 hr. LSi was then extracted from the same aliquot by HF digestion at room temperature for 48 hr. For both digests, the dissolved silicic acid (DSi) concentrations of the resulting solutions were analyzed according to Nelson et al. (1989) with a UV-Vis spectrophotometer (Analytikjena® Spector 250 plus). DSi concentrations were also measured in the supernatant of each trap cup to account for BSi dissolution during trap deployment and were added to the BSi value determined by digestion (Hurd, 1972; Nelson and Brzezinski, 1997; Nelson et al., 1995). Several aliquots of certified reference material (GBW: marine sediment, NRCC) were digested and analyzed under the same conditions, allowing validation of Si data. GBW standard analyses averaged 28.5 ± 0.5 wt.% total Si (BSi + LSi; $n = 12$), which compares well with the community consensus concentrations of 25.2 ± 0.6 wt.%. Al, Ca, Cu, Fe, Mn, Ni, Pb, Si and Zn concentrations were measured by ICP-OES (Inductively-Coupled Plasma Optical Emission Spectrometry; Perkin-Elmer® Optima-8000) after acid digestion of ~20 mg particulate aliquots in Teflon vials by successive addition of (a) 1 mL of 65% nitric acid (HNO_3^-) followed by (b) 500 µL of 65% HNO_3^- and 500 µL HF. At each step, aliquots were heated at 150°C for 5 hr. Several reagent blanks and certified reference material (GBW) were digested and analyzed under the same conditions. Blanks were below or close to the detection limits of the instrument and the percentage recovery obtained for the certified materials indicated accurate digestion and quantitative analysis for all elements (Table S1 in Supporting Information S1).

Dry material collected in acrylic traps deployed at 1,000 m on the drifting mooring line at Station 10 was filtered onto 0.2 µm polycarbonate filters, rinsed with distilled water and dried at room temperature. Filters were then coated with gold and observed using a Phenom scanning electron microscope at 10 kV.

2.2.2. Grain Size Distribution of Seafloor Sediments

Grain size of sediments was determined at the Center de Formation et de Recherche sur les Environnements Méditerranéens (CEFREM; France) laboratory using a Malvern Mastersize 3000 laser granulometer (precision ± 3%). Prior to measurement, dry sediments were homogenized, diluted in distilled water in order to achieve the concentration required by the software (i.e., 5%–20% obscuration) and ultrasonicated for 5 min. Since the number distribution may underestimate the larger particles, a particle size distribution based on a spherical equivalent volume model was used. The size of a particle was then represented by the diameter of an equivalent sphere of equal volume.

2.2.3. Sedimentation Rates of Seafloor Sediments

Sedimentation rates were determined using ^{210}Pb, a natural decay-product of ^{226}Ra with a half-life of 22.3 years ^{210}Pb deposited at the seabed by sedimentation is referred to as ^{210}Pb in excess ($^{210}Pb_{XS}$) relative to that found within sediment. Considering constant flux and accumulation rate (Robbins and Edgington, 1975), sedimentation rates were derived from the decrease of $^{210}Pb_{XS}$ activities with depth according to the following formula:

$$[^{210}Pb_{XS}]_z = [^{210}Pb_{XS}]_0 * \ e^{(-z(\lambda/SAR))} \quad (1)$$

with $[^{210}Pb_{XS}]_0$ and $[^{210}Pb_{XS}]_z$; the excess ^{210}Pb activities at the water-sediment interface and at depth z, respectively; λ, the nuclide decay constant and SAR, the sediment accumulation rate. The activities of ^{210}Pb and ^{226}Ra were determined at the Environnements et Paléoenvironnements Océaniques et Continentaux (EPOC; France) laboratory on dry sediments using a low background, high efficiency well-type gamma spectrometer (CANBERRA; Schmidt et al., 2014).

2.3. Composition of the Exported Particles and Sediments

The elemental analyses described above were used to determine the four main fractions of the collected sinking and sedimented material: organic matter (OM), calcium carbonates ($CaCO_3$), opal and lithogenic. The OM fraction was calculated from POC concentrations as 2.199 × POC (Klaas and Archer, 2002). The $CaCO_3$ fraction was estimated from PIC as $CaCO_3$ = PIC × 8.33 (Verardo et al., 1990). PIC was preferentially used, as the method from Ca tended to overestimate the $CaCO_3$ fraction on some samples (>100 wt.% of total collection weight; Table S2 in Supporting Information S1), likely due to the presence of lithogenic Ca. The opal fraction was determined from BSi concentrations as Opal = BSi × 2.4 (Mortlock and Froelich, 1989). Finally, the lithogenic fraction was determined through the mass balance method (Wefer and Fischer, 1993), by subtracting the sum of the above three fractions from the total collection weight. This method was preferentially chosen in view of the potential bias of using lithogenic tracers (LSi or Al) in this region, as these two elements can be significantly enriched or depleted through volcanic or hydrothermal activity, as discussed in Section 4.3.

2.4. Trace Metal in Sinking Particles and Seafloor Sediments

2.4.1. Calcium Carbonate-Free Basis

The bulk metal cconcentration was corrected for biogenic calcium carbonate concentration, following the approach described by German et al. (1997). Indeed, as $CaCO_3$ contains very low levels of trace elements, it can dilute the metal contribution of the collected material. Prior to any interpretation, the concentration of an element (E) was corrected on a calcium carbonate-free basis (cfb) following:

$$[E]_{cfb} = \frac{[E]}{(100 - \%CaCO_3)} \quad (2)$$

2.4.2. Metal Content

$[E]_{cfb}$ of sinking and sedimented material was compared to the concentrations of reference pelagic clays sampled in the Pacific Ocean ("pc"; Table 2; Li and Schoonmaker, 2003; Sayles and Bischoff, 1973) using two distinct methods: enrichments factors (EF) and metal excess (XS).

Table 2
Elemental Enrichment Factors (E_{EF}) of Metals in Sinking Material Relative to Aluminum (Al_{cfb}) and Average Concentrations in Reference Pelagic Clays

Sample	Fe	Mn	Cu	Zn	Ni	LSi
Station 5–1,000 m	**1.4**	*0.2*	*0.6*	**11**	1.1	**5.2**
Station 10–200 m	1.1	**5.0**	**18**	**37**	**7.3**	*0.4*
Station 10–1,000 m	1.0	*0.01*	*0.03*	*0.7*	*0.1*	**14**
Station 12–200 m	1.1	*0.02*	*0.2*	**6.1**	*0.1*	*0.2*
Station 12–1,000 m	**1.7**	*0.6*	**2.0**	**39**	**2.7**	**1.6**
Reference pelagic clays	5.9 ± 0.6	1.1 ± 0.4	469 ± 181	158 ± 12	196 ± 14	25 ± 1

Note. Enrichments relative to Pacific Ocean pelagic clays (EF > 1) are shown in bold while depletions relative to the reference (EF < 1) are shown in italics. Average concentrations and standard deviations (in wt.% for Fe, Mn and LSi and ppm for Cu, Zn and Ni) within several reference pelagic clays (from Li and Schoonmaker, 2003; Sayles and Bischoff, 1973; Taylor and McLennan, 1985) are shown at the bottom of the table. Note that the range of concentrations measured for each element in these references provides only a rough estimate of metal non-detrital enrichment in the material collected in this study. It may therefore over- or underestimate the magnitude of these enrichments.

Note. Enrichments relative to Pacific Ocean pelagic clays (EF > 1) are shown in bold while depletions relative to the reference (EF < 1) are shown in italics.

2.4.3. Enrichment Factors in Sinking Particles

For the sinking material, EF were calculated by normalizing the concentration ratio of an element $(E)_{cfb}$ to aluminum (Al_{cfb}, lithogenic tracer) to the same elemental ratio measured in pelagic clays following the formula:

$$E_{EF} = \frac{[E]_{cfb\ sample}/[Al]_{cfb\ sample}}{[E]_{pc}/[Al]_{pc}} \quad (3)$$

2.4.4. Elemental Excess in Seafloor Sediments

For seafloor sediments, metal excess relative to reference pelagic clay composition was determined by correcting $[E]_{cfb}$ for detrital inputs (German et al., 1997) assuming that this reference material was representative of a deep-sea detrital end-member. Detrital concentrations of each element were calculated according to:

$$[E]_{det} = [Al]_{cfb} * \frac{[E]_{pc}}{[Al]_{pc}} \quad (4)$$

It is important to note that this calculation assumes that all sedimentary Al originates from detrital material. However, sedimentary Al concentrations could originate from both hydrothermal and detrital sources (Massoth et al., 1998; Resing and Sansone, 1999; Von Damm, 1990). Consequently, Al normalization may have underestimated the extent of hydrothermal enrichment in our seafloor sediments (Chavagnac et al., 2008). That fraction of non-detrital origin, denoted $[E]_{XS}$, was determined by subtracting $[E]_{det}$ from $[E]_{cfb}$, as follows:

$$[E]_{XS} = [E]_{cfb} - [E]_{det} \quad (5)$$

2.5. Statistical Analysis

To determine if significant differences could be observed in the fractions of material collected at the different stations, a non-parametric Mann-Whitney test was performed. This two-tailed distribution-free test was selected due to the non-normally distributed data, previously determined through a Kolmogorov-Smirnov test. Differences were considered significant at a p-value (p) < 0.05.

3. Results

3.1. Composition of the Sinking Particles and Seafloor Sediments

3.1.1. Biogenic Particles

Three fractions of the collected material can be used as proxies for biological production: $CaCO_3$, opal and OM. It should be noted that due to the strong seasonal effect prevalent in the region (see Figure 2e–2h), the quantities

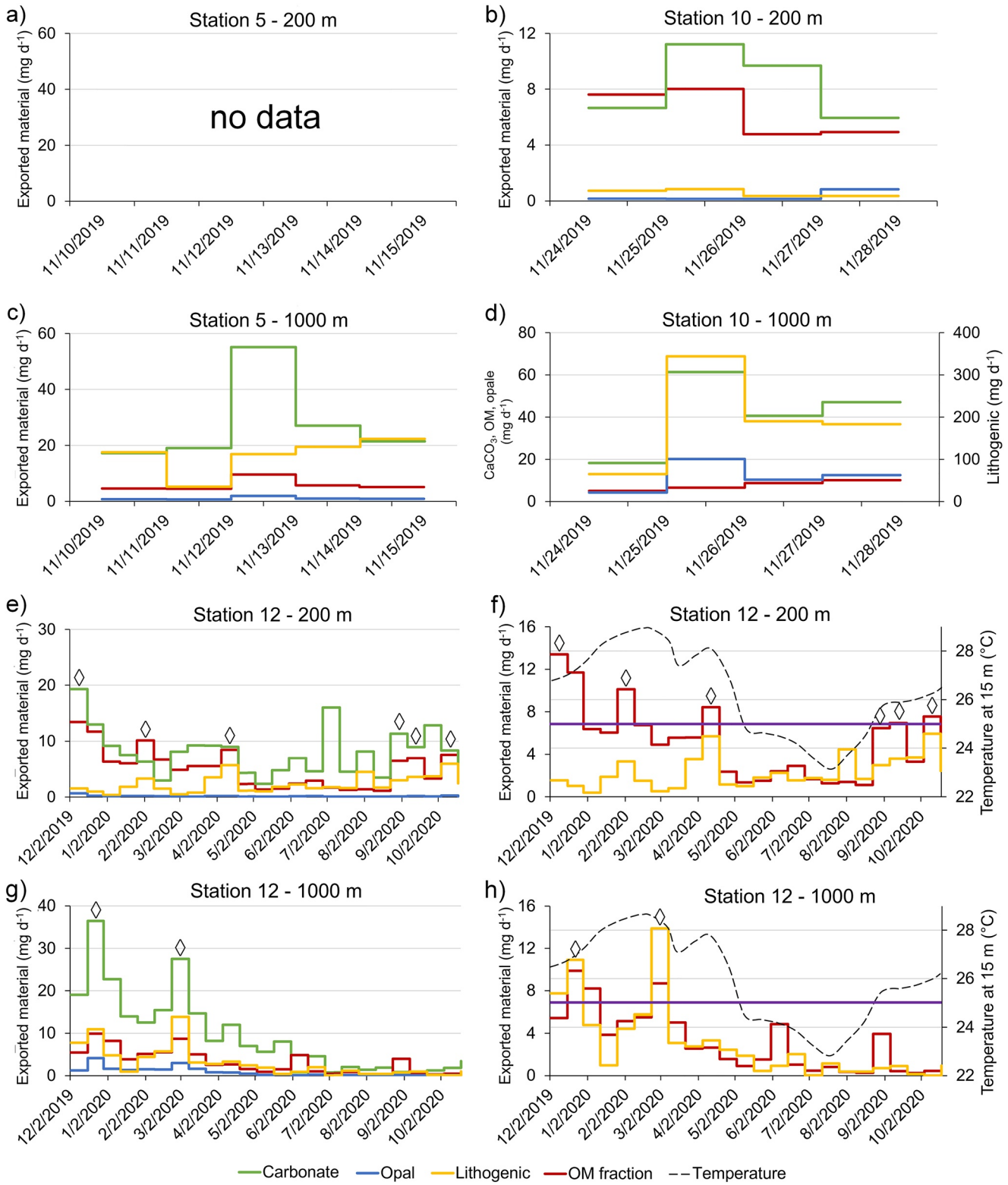

Figure 2.

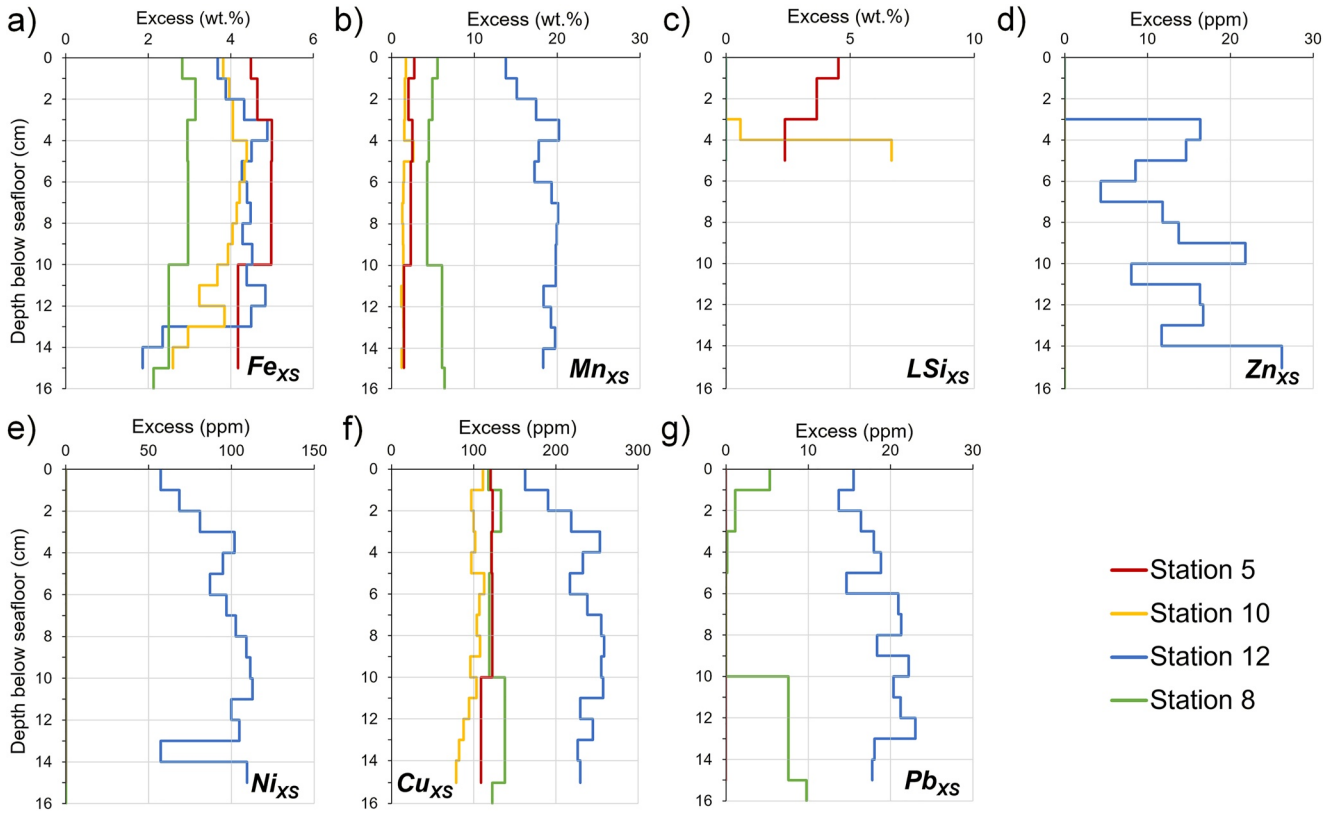

Figure 3. Excess of metal (E_{XS}) in each slice of seafloor sediments relative to the composition of reference pelagic clays: (a) iron (Fe_{XS}), (b) manganese (Mn_{XS}), (c) lithogenic silica (LSi_{XS}), (d) zinc (Zn_{XS}), (e) nickel (Ni_{XS}), (f) copper (Cu_{XS}) and (g) lead (Pb_{XS}). Excess in major elements are represented in wt.% (Fe, Mn, Si, Ca) and minor elements (Zn, Ni, Cu, Pb) in ppm.

of biological material collected in the drifting traps (4–5 days during the austral summer) will only be compared to the quantities of the same material collected in the fixed trap during the austral summer period (i.e., from December 2019 to April 2020), and not over the whole year.

3.1.1.1. Exported Particles

$CaCO_3$ was the most abundant biogenic component of the exported material during the austral summer (on average over stations and depths: 48–59 wt.%; Figure S2 in Supporting Information S1) if station 10 at 1,000 m is excluded (average 17 wt.%). The amount of $CaCO_3$ collected during the austral summer averaged 18 ± 10 mg d^{-1} at all stations and depths, with a significantly higher accumulation at 1,000 m ($\sim 25 \pm 12$ mg d^{-1}; $p < 0.05$; Figure 2) than at 200 m ($\sim 9 \pm 3$ mg d^{-1}). In comparison, quantities collected during the austral winter at station 12 (fixed mooring) were much lower ($\sim 5 \pm 3$ mg d^{-1}), particularly at 1,000 m ($p < 0.05$). At this station, only two $CaCO_3$ peaks were observed at 1,000 m (in December and February) while they were more frequent at 200 m. Opal fraction was the smallest biogenic component of the sinking material during the austral summer (1–5 wt.%; Figure S2 in Supporting Information S1), regardless of station and collection depth ($\sim 2.1 \pm 2.4$ mg d^{-1}; Figure 2), with a significantly higher quantity collected at 1,000 m than at 200 m ($p < 0.05$). In comparison, opal quantities collected during the austral winter were lower ($\sim 0.12 \pm 0.05$ mg d^{-1}) although similar at both collection depths ($p > 0.4$). Two opal peaks, matching the $CaCO_3$ peaks in December

Figure 2. Temporal dynamics of exported material (mg d^{-1}) in drifting (a)-(d) and fixed (e)-(h) sediment traps: organic matter (red line), calcium carbonate (green line), opal (blue line) and lithogenic fraction (yellow line). Shown on the different panels are: station 5 at 200 and 1,000 m (a), (c), station 10 at 200 and 1,000 m (b), (d) and station 12 at 200 and 1,000 m (e), (g). Note that the lithogenic fraction is represented on a different y-label for station 10–1,000m (c). Panels (f) and (h): organic and lithogenic material (left y-label) versus temperature at 15 m (right *y*-label; gray dotted line) for both traps at station 12. The diamond on panels (e)-(h) indicates that the peaks of at least two fractions ($CaCO_3$, lithogenic, OM, opal) overlapped on this sampling date. The purple line delineates a temperature of 25°C. Temperature data were extracted from the World Ocean Atlas database (Locarnini et al., 2018): average monthly temperature over the period from 2005 to 2017 at 15 m, near station 12. Note that no significant annual variation in temperature was observed (12-year monthly standard deviation ranging from 0.16 to 0.67°C). Cumulative histograms of these fractions are shown in Figure S2 in Supporting Information S1.

and February, were observed at 1,000 m at the fixed mooring station. OM fraction was the second most abundant biogenic component at 200 m during the austral summer (40–41 wt.%; Figure S2 in Supporting Information S1), with similar amounts of material collected at all stations and depths (~6.4 ± 2.2 mg d^{-1}, $p > 0.09$, Figure 2). However, these quantities decreased significantly during the austral winter at both deployment depths ($p < 0.05$). At station 12, OM peaks were observed from October to May and from December to February in the traps deployed at 200 and 1,000 m, respectively. At 1,000 m on the same site, those peaks matched those of opal and $CaCO_3$ (Figure 2g).

3.1.1.2. Seafloor Sediments

The proportion of $CaCO_3$ in seafloor sediments was very low (<5 wt.%) at most stations, except at station 12 (64 ± 1 wt.%, $p < 0.05$, Table 1). Although present in low proportions (10 ± 2 wt.%), opal was the most abundant biogenic component in seafloor sediments, with no difference between stations ($p > 0.05$). OM proportion was less than 1 wt.% for all stations and did not differ between stations ($p > 0.05$).

3.1.2. Lithogenic Material

3.1.2.1. Exported Particles

The smallest amount of lithogenic material was collected at 200 m at station 10 (~0.5 ± 0.2 mg d^{-1}; 3 ± 1 wt.%; Figure 2 and Figure S2 in Supporting Information S1). In contrast, at the same station at 1,000 m, the lithogenic material was up to four orders of magnitude higher (maximum of 344 mg d^{-1}; 75 ± 3 wt.%). Large amounts were also collected at 1,000 m at station 5 (~16 ± 4 mg d^{-1}; 33 ± 11 wt.%), albeit significantly lower (by a factor of 20, $p = 0.03$). In comparison, at station 12 (fixed mooring), lithogenic amounts were lower throughout the year ($p < 0.02$) and of the same order of magnitude in both traps (on average for the two traps deployed at station 12: ~2.6 ± 1.9 mg d^{-1}; ~16 ± 7 wt.%; $p = 0.2$). At 200 m at station 12, the observed lithogenic peaks coincided with the majority of OM peaks, except between May and September. Notably, two lithogenic peaks (up to 14 mg d^{-1}), matching those of all biogenic components ($CaCO_3$, opal, OM), were observed in December and February at 1,000 m.

3.1.2.2. Seafloor Sediments

The lithogenic fraction was the most abundant fraction in the seafloor sediments at stations 5, 8 and 10 (88–90 wt.%, Table 1). In contrast, at station 12, the lithogenic fraction was only 23 ± 3 wt.% ($p < 0.001$), due to the dilution effect by the high $CaCO_3$ fraction.

3.2. Trace Metal Content and Enrichment Factors

Metals in sinking particles and in seafloor sediments are presented in Figurs. S3 and S4 in Supporting Information S1.

3.2.1. EF in Exported Material

Enrichment of Zn (Zn_{EF}) was detected in the material collected from all sediment traps compared to reference pelagic clays (x6-39; Table 2), except at 1,000 m at station 10. Slightly elevated Fe_{EF} was estimated at 1,000 m at stations 5 and 12 (×1.5–1.8). No Mn_{EF} was detected in traps, except at 200 m at station 10 (×7). Significant Ni_{EF} (x3-7) were observed at 1,000 m at station 12 and at 200 m at station 10. Cu_{EF} was measured only in the material collected at station 10 at 200 m and station 12 at 1,000 m (×18 and ×2, respectively). LSi_{EF} was estimated at 1,000 m at all stations, up to a factor of 14 (station 10).

3.2.2. Elemental Excess in Seafloor Sediments

Several metals were in excess in the sampled sediments relative to the composition of reference pelagic clays of the Pacific (Figure 3). At all depths, sediments showed marked Fe_{XS}, although significantly lower at station 8 (on average ~3 wt.% Fe_{XS}, $p < 0.05$) than at stations located in the Lau Basin (up to ~5 wt.% Fe_{XS}). Significant Mn_{XS} (~2–20 wt.%) and Cu_{XS} (~100–230 ppm) were detected in all sediments, with the highest excess measured at station 12 ($p < 0.05$). This station also had the unique characteristic of displaying Ni_{XS} (~100 ppm), Zn_{XS} (~10 ppm) and Pb_{XS} (~20 ppm) while no excess was detected at the other stations (excluding small occasional Pb_{XS} within the station 8 profile; up to 10 ppm). High LSi_{XS} were measured at stations 5 (~5 wt.%) and 10 (up to ~7 wt.%).

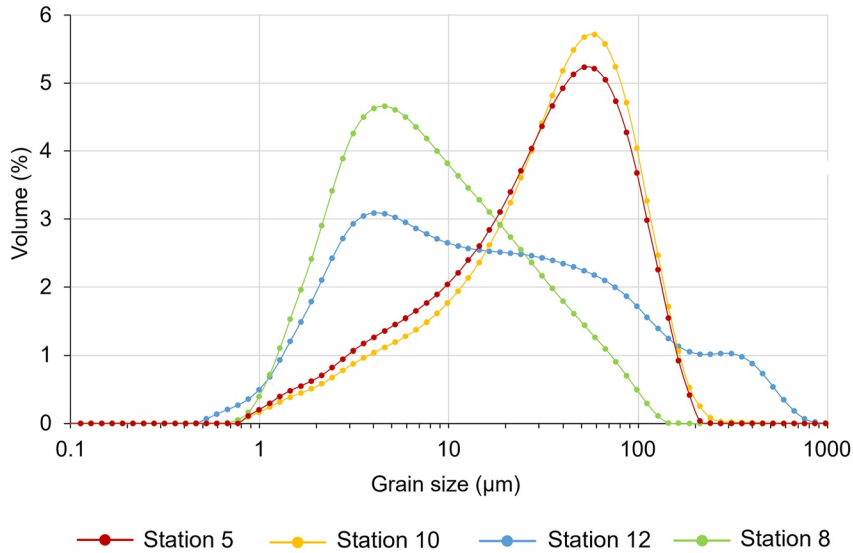

Figure 4. Grain size distribution averaged for all sediment slices at each station. The distribution for each sediment slice is shown in Figure S5 in Supporting Information S1.

3.3. Grain Size Distribution of Seafloor Sediments

The smallest particle sizes, mainly between 2 and 16 µm, were measured at station 8 (Figure 4). Larger particles were identified at stations 5 and 10, primarily between 30 and 110 µm. A wide range of particle sizes was measured at station 12, mainly ranging from 1 to 310 µm and up to 976 µm.

3.4. Sedimentation Rate of Seafloor Sediments

^{210}Pb and $^{210}Pb_{XS}$ activities ranged from 11 to 290 mBq g^{-1} and from 1 to 259 mBq g^{-1}, respectively (Figure S6 in Supporting Information S1). Values of $^{210}Pb_{XS}$ decreased exponentially with depth in the sediments cored at stations 5, 10 and 12, reaching negligible levels at about 6–10 cm, depending on the core considered. This was not the case for the core from station 8, which still exhibited high $^{210}Pb_{XS}$ in the 10–15 cm sediment layer, associated with the highest ^{226}Ra values measured in the studied cores (100–200 mBq^{-1}). Such high ^{226}Ra activities may be related to hydrothermal enrichment. Indeed, it could be suspected that below 3–5 cm, total ^{210}Pb activities correspond to a combination of $^{210}Pb_{XS}$ and ^{210}Pb ingrowth from Ra enrichment: the deepest $^{210}Pb_{XS}$ activities are then not reliable to estimate the sedimentation accumulation rate. Other explanations for these patterns, such as bioturbation, were considered but excluded as they differ from the ^{210}Pb and ^{226}Ra bioturbation profiles observed in previous studies (Sakaguchi et al., 2011). For stations 5, 10, and 12, sediment accumulation rates ranged from 47 to 61 cm kyr^{-1} (Table 1). For station 8, considering only the first two levels of the profile, it was possible to calculate a sedimentation rate of 58 cm kyr^{-1}, close to those obtained at the other stations.

4. Discussion

Sediment traps have been a standard tool for measuring sinking particle fluxes for decades, but uncertainties remain as to their collection efficiency (e.g., Baker et al., 2020; Buesseler et al., 2007; Butman, 1986; Gardner, 1980; Hargrave and Burns, 1979). In the present study, efforts were made to accurately collect sinking particles as detailed in Text S1 in Supporting Information S1.

4.1. Non-Vertical Sinking of Particles Collected in the Fixed Sediment Trap

The peaks of the different fractions composing the material were not simultaneously observed in the traps deployed at 200 and 1,000 m at the same site (Figure 2), as usually occurs in similar studies (e.g., Guieu et al., 2005; McCave, 1975; Wefer and Fischer, 1993). The temporal shift of these peaks would indicate that particles would be collected at 1,000 m, 30–56 days after being collected at 200 m (see relevant peaks in Figure S7 in Supporting

Information S1). This observation suggests that while sinking toward the seafloor, the particles were subject to horizontal transport, in view of the westward main current (Tilliette et al., 2022). Thus, the collected particles sank progressively from the photic layer near the arc (0–150 m) while being horizontally advected toward the location of the fixed mooring. The time lag between the collection of particles at 200 and 1,000 m is due to depth-dependent physical dynamics (faster current velocity at surface and influence of mesoscale structures predominant in the sub-region; Rousselet et al., 2018) as well as the travel time of the water masses, much faster at 200 m than at 1,000 m. Indeed, Lagrangian simulations through Ariane software showed that sinking particles originating from the Tonga Arc require 61 and 103 days to reach the fixed trap site at 200 and 1,000 m, respectively (Grima, pers. comm., 2022). This is consistent with the time lag between the observed peaks at 200 and 1,000 m. This reasoning suggests that an important portion of the sinking material collected in the sediment traps at station 12 would originate from the photic layer near the Tonga Arc, influenced by shallow hydrothermal fluids, as discussed in Section 4.3. Nevertheless, the finding of a non-vertical sinking of suspended particles highlights the importance of employing numerous precautions when interpreting sediment trap data, especially when estimating POC transfer efficiency, which would then be completely spurious in such a case.

4.2. Biogenic Components of Sinking Particles and Seafloor Sediments During the Austral Summer

4.2.1. Summary of Production at Studied Stations During Austral Summer Conditions

During the TONGA cruise in the austral summer (Bonnet, pers. comm., 2022), high rates of primary production (PP) were estimated in the Lau Basin (up to 145 mmol C m^{-2} yr^{-1} at station 10; Table S3 in Supporting Information S1). This production was largely supported by cyanobacteria (~70% of total chlorophyll-*a*), primarily diazotrophs such as *Trichodesmium* that led to high N_2 fixation rates (up to 2727 µmol N m^{-2} d^{-1} at station 5). A significant contribution of coccolithophores was also estimated (~25%) while diatoms and dinoflagellates represented less than 10% of total chlorophyll-*a* in the Lau Basin. In comparison, PP and N_2 fixation were much lower at station 8 (<35 mmol C m^{-2} d^{-1} and 225 µmol N m^{-2} d^{-1}, respectively) and supported predominantly by non-diazotrophic cyanobacteria (Bonnet, Guieu et al., 2023).

4.2.2. Calcium Carbonate

The dominant source of $CaCO_3$ (mainly calcite) comes from a wide variety of pelagic organisms such as coccolithophores and foraminifera (Morse et al., 2007). The high $CaCO_3$ contents measured at all stations in sediment traps during the austral summer were consistent with the high productivity of the Lau Basin estimated at the same period (see Section 4.2.1). Interestingly, more $CaCO_3$ was collected at 1,000 m than at 200 m, certainly due to the fast sinking rates of $CaCO_3$ skeletons (Turner, 2002; Zhang et al., 2018; Ziveri et al., 2000). The high levels of $CaCO_3$ measured in the seafloor sediments at station 12 suggest good preservation of the sinking material on the seafloor in agreement with values reported in the literature from the region (Table 1; Zhang et al., 2022). The lower $CaCO_3$ preservation in the seafloor sediments at station 8 can easily be explained by the seafloor depth (5326 m), far below the calcite compensation depth (CCD; Figure S8 in Supporting Information S1). Conversely, the seafloor at stations 5 and 10 (~2000 m), located above the lysocline and therefore the CCD, cannot explain the observed patterns. As the Tonga Arc harbors an intense hydrothermal activity (see Section 1), its seafloor may be characterized by strong physical and chemical gradients (temperature, oxygen levels, multiple forms of chemical energy) and encompass a diverse range of habitats for microbial life (Karl, 1995). It would thus harbor enormous biomasses and productivities relative to other regions of the deep ocean (Zierenberg et al., 2000), which may explain the low $CaCO_3$ content of the sediments at stations 5 and 10.

4.2.3. Opal

Opal minerals originate from a wide variety of silica-skeleton organisms, primarily diatoms (Tréguer et al., 1995). As expected from the low proportion of diatoms during the austral summer in the region (see Section 4.2.1), the opal fraction was the least abundant fraction in the sinking material during this season. As for $CaCO_3$, the larger quantity of opal collected at 1,000 m than at 200 m can be explained by the rapid fall rate of the opal skeletons (Bodungen et al., 2013; Turner, 2002). In comparison, the greater proportion of opal found in the seafloor sediments may be explained by the higher preservation efficiency of BSi relative to OM and $CaCO_3$; degradation of these other fractions may therefore account for the increasing opal proportion in sediments (Emerson and Hedges, 1988; Gersonde et al., 2005). Furthermore, opal sinks at rates fast enough to contribute significantly to seafloor sediments, in contrast to other biogenic fractions (Sarmiento and Gruber, 2006).

Table 3
Average Boström Indexes Measured in Sinking Particles and Seafloor Sediments for Each Station

Station	Depth	Boström index	
-	(m)	Mean	sd
Station 5	1,000	50.6	0.4
	Seafloor	39.7	1.7
Station 10	200	23.8	6.1
	1,000	66.6	0.5
	Seafloor	45.2	1.3
Station 12	200	55.6	9.7
	1,000	42.7	6.0
	Seafloor	15.9	0.9
Station 8	Seafloor	37.8	1.0

Note. Indexes were measured as follows: $100 \times [Al_{cfb}/(Al_{cfb} + Mn_{cfb} + Fe_{cfb})]$ (Boström et al., 1969). The index for detrital pelagic sediments is 66 (Kyte et al., 1993; Plank et al., 2007). An index below 45 reflects fallout from a dispersed hydrothermal plume, having a high contribution of Fe-Mn oxides mixed with decreasing proportions of detrital material as distance from the source decreases (Chavagnac et al., 2008; Dymond, 1981). An index below 15 reflects near-vent sulfide debris (Mills et al., 1993). The set of index values in each trap cup and sediment slice is available in the supplementary material (Table S4 in Supporting Information S1).

4.2.4. Organic Matter

The abundant proportion of OM collected in all traps during the austral summer can easily be linked to the seasonal productivity of the Lau Basin, which hosts shallow hydrothermal sources driving a ~360,000 km^2 productivity hotspot, mainly supported by diazotrophs such as *Trichodesmium* (up to 84% of total export; Bonnet, Guieu et al., 2023). This large export matched well with the export of lithogenic material, except during the austral winter period despite the high supply of lithogenic material throughout the year. This may be linked to the thermal fitness of *Trichodesmium*, which only grows at temperatures >25°C (Carpenter & Capone, 1992), reached in the Lau Basin between September and April (Figures 2f and 2h). Thus, the high amount of OM exported in the Lau Basin appears to depend on lithogenic-derived nutrient inputs, suggesting that this material, most likely of hydrothermal origin (Bonnet, Guieu et al., 2023; Tilliette et al., 2022), would drive the high diazotroph-mediated production. As expected, only a minor proportion of OM was sequestered in the seafloor sediments, this material being remineralized during its transport to the deep ocean (Boyd & Trull, 2007 and reference therein).

Taken together, these data illustrate the high biological productivity previously reported in the Lau Basin during the austral summer season and mainly supported by calcareous (i.e., $CaCO_3$) and diazotrophic (i.e., OM) species (Bonnet, Guieu et al., 2023). These biological particles were intimately linked to the influx of lithogenic material largely originating from the Tonga Arc, renowned for its shallow hydrothermal activity (e.g., Massoth et al., 2007; Tilliette et al., 2022). This suggests that surface production is closely linked to hydrothermal supply in the Lau Basin photic layer. To confirm the implication of hydrothermalism in triggering the biological response, the origin of lithogenic particles will be resolved in the subsequent section.

4.3. Characteristics of the Metallic Component in Sinking Particles and Seafloor Sediments

4.3.1. Origin of Trace Metals in Sinking Particles and Link With Surface Biology

Likely largely originating from the Tonga Arc area (see Section 4.1), the lithogenic material collected in sediment traps was highly enriched in several metals compared to reference pelagic clays. Given the preponderance of shallow and deep hydrothermal sources in the Lau Basin (e.g., Anderson et al., 2021; Baker et al., 2019; Beaulieu & Szafrański, 2020; Lupton et al., 2004; Massoth et al., 2007; Tilliette et al., 2022) and the similar patterns of biological and lithogenic fractions during the austral summer period, the question of the origin of this metal excess is of utmost interest.

Hydrothermal material has a particular signature characterized by low Al content but rich in Fe and Mn, as well as many other metals such as Cu, Zn, Ni, and Pb (Boström et al., 1969; Boström & Peterson, 1969; Cronan, 1972). However, particularities exist for these elements, as some of them, such as Cu and especially Ni and Zn, decrease dramatically with distance from the source relative to Fe, due to their rapid removal by sulfide-bearing phases (Trocine and Trefry, 1988). A convenient way to discriminate material of hydrothermal origin is based on the Boström index using Al_{cfb}, Fe_{cfb}, and Mn_{cfb} concentrations (Boström et al., 1969). Its value provides a clear indication of the material provenance: a value close to 66 would indicate a clastic detrital sediment (Kyte et al., 1993; Plank et al., 2007) while values <45 would indicate a significant hydrothermal component (Chavagnac et al., 2005; Humphris et al., 1995; Mills and Elderfield, 1995). The closer the value is to 0, the more hydrothermal the material is and thus the closer the hydrothermal source (Dymond, 1981; Mills et al., 1993). In this study, indexes with particular and diverse signatures were determined, suggesting a hydrothermal origin, remote or not, of the lithogenic material collected at some of the stations studied (Table 3).

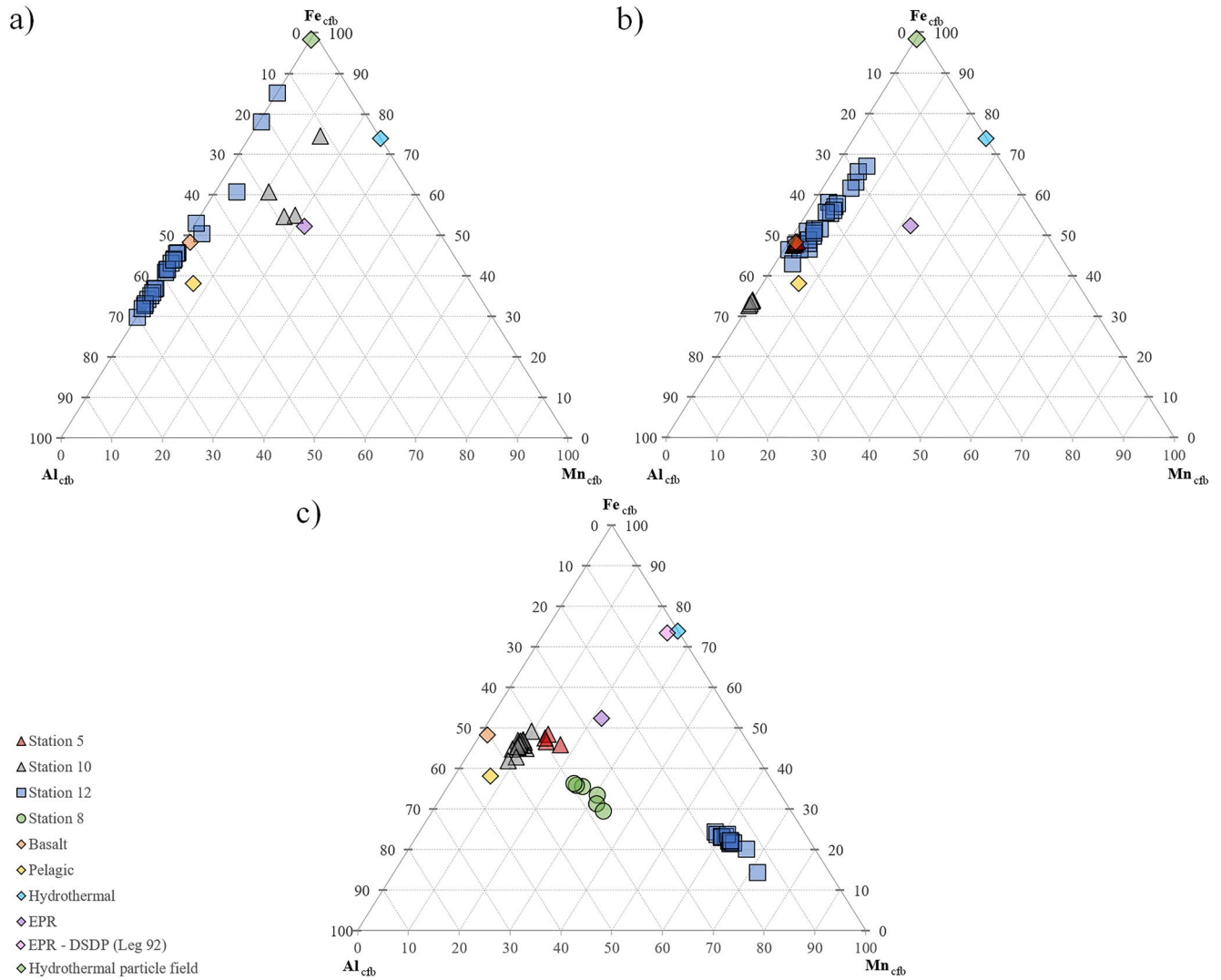

Figure 5. Fe_{cfb}, Mn_{cfb}, and Al_{cfb} ternary diagrams for sinking material collected at (a) 200 m and (b) 1,000 m and for (c) seafloor sediments. Also shown for comparison are some reference materials such as basalt (Japan Basalt, GSJ; Imai et al., 1995), reference pelagic clays (see Table 2), a hydrothermal vent solution (Li and Schoonmaker, 2003), a reference sedimentary material from the East Pacific Rise (EPR; Barrett et al., 2021; Nohara and Yokoto, 1978) and a hydrothermal particle field (Edmonds and German, 2004).

4.3.1.1. Along the Tonga Arc (Small Scale)

Stations 5 and 10 are located along the Tonga Arc, which hosts a multitude of active hydrothermal vents (e.g., Beaulieu & Szafrański, 2020; Lupton et al., 2004; Massoth et al., 2007). About 15 km from the location of each of the drifting mooring lines, a shallow hydrothermal source was identified during the TONGA cruise at ~300 m at station 10 and at ~200 m at station 5 (Tilliette et al., 2022).

Station 10. Station 10 revealed materials with distinctive signatures depending on sampling depth. At 200 m, the Boström index revealed a clear signature of a fairly close hydrothermal source with Fe-Mn-rich lithogenic particles (Table 3, Figure 5a), similar to metalliferous sediments sampled downstream of the Rain hydrothermal vent on the Mid-Atlantic ridge (Cave et al., 2002). Such index is in agreement with the identification, ~15 km away from the drifting mooring initial position, of a shallow source exhibiting multiple acoustic anomalies and high DFe concentrations (Tilliette et al., 2022). Consistently, Cu_{EF}, Zn_{EF} and Ni_{EF} were detected in the trap (Table 2). However, biological (intracellular) inputs through OM must partly contribute to these high enrichments, since some metals, notably Zn, are highly abundant in phytoplankton ($[C_{106}N_{16}P_1]_{1000}Fe_{11.9}Zn_{1.27}Cu_{0.15}$; Ho et al., 2003; Redfield et al., 1963; Zhang et al., 2018). Based on these elemental ratios, the contribution of the biological

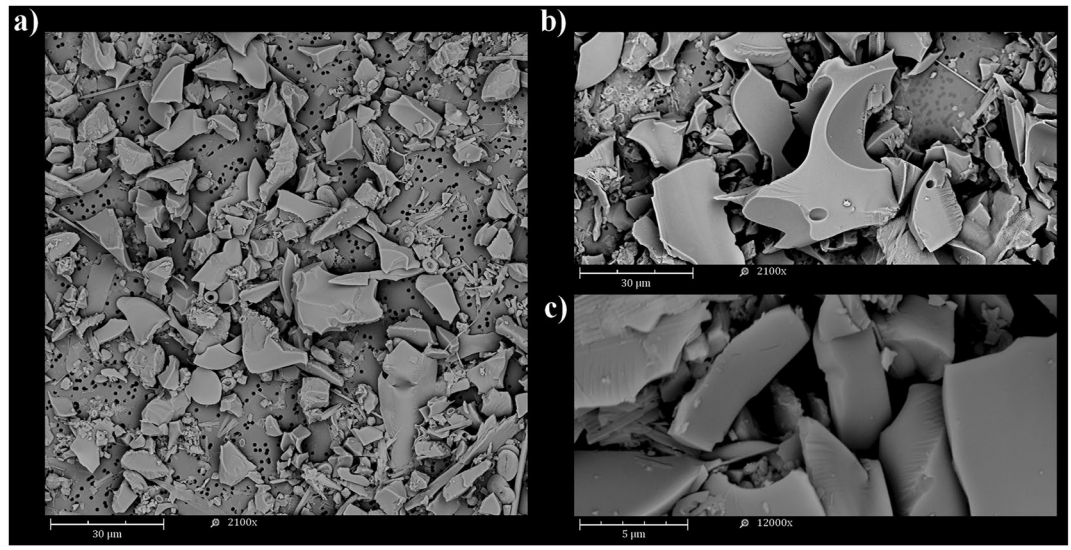

Figure 6. Scanning electron microscopy views of dry material from samples collected in the 1,000 m-trap at station 10 where basaltic glass was recovered (magnification (a, b): ×2,100 and (c): ×12,000).

fraction to Zn_{EF} can be considered negligible (~3%). Nevertheless, all these arguments point out to a hydrothermal origin of a large part of the lithogenic material collected at 200 m, which likely triggered surface biological production at this station during the austral summer.

At 1,000 m, a Boström index typical of conventional detrital material was measured (Table 3), although the Al-Fe-Mn signature of the collected material seems to differ from that of the reference pelagic clays (Figure 5b). Yet, station 10 is located close to the Late'iki submarine volcano, which erupted a month prior to the cruise. This surtseyan eruption created a new island, baptized New Late'iki, which eroded in just 2 months. This erosion released a large amount of volcanic material into the water column, which was detectable until December 2020 (Plank et al., 2020). Accordingly, a large abundance of basaltic glass, likely from this eruption, was collected in the 1,000 m-trap deployed at this station (Figure 6). Indeed, the angular shape of this volcanic material indicates its recent origin and freshness, since remobilized volcanic particles would display more rounded angles. The detrital-like Boström index can therefore be attributed to the predominance of volcanic-derived particles, a material reported as Mn-poor but Fe and Al-rich (Figure 5b; e.g., Almirón et al., 2021; Fiantis et al., 2010; Leonelli et al., 2007; Naji and Asi, 2008; Oskarasson, 2010; Razzhigaeva et al., 2009; Tchakoute Kouamo et al., 2012). LSi_{EF} at 1,000 m provides further evidence, as this element has been reported to be enriched in volcanic material relative to pelagic ones (Bailey, 1993; Fiantis et al., 2010; Li and Schoonmaker, 2003; Sayles and Bischoff, 1973). Thus, a mixture of volcanic, hydrothermal and detrital material probably prevailed at 1,000 m. Given the large amount of material ejected following the Late'iki eruption and the biological response to lithogenic inputs in the austral summer, it is interesting to consider a possible co-fertilization of biology by both hydrothermal and volcanic processes. However, such volcanic fertilization is unlikely as no volcanic signature was detected in the 200 m-trap (i.e., no LSi_{EF}) and recent studies in the region have demonstrated that volcanic material, particularly basaltic glass, is poorly bioavailable and does not generate a significant biological response (Whiteside et al., 2021, 2023).

Station 5. The shallow hydrothermal source identified at ~200 m at station 5 during the TONGA cruise was a very active site showing typical acoustic and chemical anomalies such as low pH, low O_2 concentrations and high levels of DFe, DMn, CH_4, CO_2 and H_2S (Tilliette et al., 2022). At 1,000 m, the moderate Boström index of the collected lithogenic particles likely reflected a mixture of (a) hydrothermal material from shallow hydrothermal plumes (Tilliette et al., 2022), notably supported by strong Fe_{EF} and Zn_{EF} (Table 2, Figure 5b), (b) volcanic material from New Late'iki erosion, according to the westward main current, supported by LSi and Al enrichments as well as Mn depletion (Figure 5b and Table 2), and (c) detrital material. Thus, the lithogenic material collected at 1,000 m appears to have both volcanic and hydrothermal origins. As volcanic material is poorly bioavailable (Whiteside et al., 2021, 2023), it can be concluded that the large quantities of biological material collected

during the austral summer, in particular OM and $CaCO_3$, result from the presence of a shallow hydrothermal source along the Tonga Arc (Tilliette et al., 2022). This source released high amounts of lithogenic material rich in numerous metals essential for phytoplankton growth, such as Fe, thereby sustaining significant biological productivity. However, as the 200 m-trap did not work (see Section 2.1), its deployment needs to be renewed to confirm that the hydrothermal material identified at 1,000 m originates exclusively from the near-surface source identified, or whether additional deeper sources exist.

4.3.1.2. Along the Lau Ridge (Large Scale)

Station 12 was positioned sufficiently far from the identified shallow hydrothermal sources on the Tonga Arc to incorporate their effect on a regional scale. At 200 m, the lithogenic material collected exhibited a rather high Boström index, but still lower than detrital material, reflecting the likely remote impact of the shallow sources identified along the Tonga Arc (~200 km from station 12). These sources supply low but still significant concentrations of metals up to the photic layer of the Lau Ridge, particularly Fe (Figure 5a), in line with the main westward current reflecting their impact on a regional scale. The Boström index variability over the year suggests an important role of subsurface dynamics in delivering lithogenic material up to station 12 (Table S4 in Supporting Information S1). Consistent with this distal hydrothermal contribution, no Cu_{EF} and Ni_{EF} were detected in this trap. Similar to station 10, a small proportion of the Zn_{EF} estimated at station 12 can be partially attributed to OM supplies (up to 2% biologically-derived Zn, depending on the collection period). Thus, the lithogenic material collected at 200 m at station 12 appears to have a hydrothermal origin, similarly to the stations along the Tonga Arc. This observation suggests that hydrothermal inputs from the Tonga Arc into the photic layer can fertilize surface biology on the scale of an entire ocean basin (i.e., from the Tonga Arc to the Lau Ridge—200 km), as long as the optimal conditions for diazotroph growth (i.e., temperature), reached during the austral summer period in the region, are satisfied.

The lower Boström index measured at 1,000 m than at 200 m at station 12 reflects a greater influx of hydrothermal material, especially Fe, from distal shallow and/or deep source(s) likely located along the Tonga Arc (Figures 5b and 5Table 3). A part of the lithogenic particles collected were also of volcanic origin, in view of the Mn depletions as well as Al, Fe and LSi enrichments, thus impacting the measured index (i.e., increasing it). These LSi_{EF} likely originated from the Late'iki eruption (mid-October 2019; Plank et al., 2020) and the subsequent fast erosion of the newly created island (within two months post-eruption), consistent with the main western current potentially carrying basaltic glass to station 12 (Tilliette et al., 2022). This hypothesis is supported by the travel time of particles from station 10 (about 15 km away from New Late'iki) to the fixed trap site at station 12 estimated to be about a hundred days at 1,000 m by the Ariane Lagrangian dispersion tool (Grima, pers. comm., 2022; see Section 4.1). Indeed, no LSi_{EF} was detected at 1,000 m at station 12 about 150 days after the submarine volcano eruption ($\times 0.4 \pm 0.3$ between March and October 2020), and about 70 days after the island disappearance due to erosion, in agreement with the estimated dispersal times at 1,000 m from the Tonga Arc to the fixed mooring site. Thus, as for station 5, the lithogenic material collected at 1,000 m is derived from volcanism as well as from shallow and/or deep hydrothermalism. However, only material of hydrothermal origin may explain the substantial biological production measured remotely of the Tonga Arc during the austral summer period.

4.3.2. Origin of Trace Metals in Sediments

Mirroring the material collected in sediment traps, the lithogenic material collected in the sediments was highly enriched in metals. Given the intense hydrothermal and volcanic activity prevalent in the region (see Section 4.3.1 and references therein), it is important to question the potential origins of these metal excesses, in particular to determine whether or not the sources feeding the sediments differ from those feeding the water column.

4.3.2.1. In the Lau Basin

Station 10. In the sediments at station 10, a lower Boström index than that of material collected at 1,000 m indicated the presence of a deep (>1,000 m), rather distal, hydrothermal source feeding the sediments with high Fe, Cu and, to a lesser extent, Mn contents (Table 3, Figures 3 and 5c). Indeed, although volcanic material (i.e., increasing the index) was also present within the sediments according to LSi_{XS} estimates, the decrease of the index value seems to indicate additional hydrothermal input at depths >1,000 m. The source(s) of these inputs appear(s) to be at a reasonable distance from the station, given the particle size typical of distal transport (1–100 μm; Feely et al., 1987, 1990; Lou et al., 2020). Consistently, estimated sedimentation rates were 94–470 times higher than those of pelagic sediments (average 0.1–0.5 mm kyr^{-1}; Li and Schoonmaker, 2003; Piper, 2005) and in

the range of those measured in hydrothermally-influenced areas accumulating to several cm kyr^{-1} (Cave, 2002; Cave et al., 2002; Dutkiewicz et al., 2016; Mahiques et al., 2011). Such rates indicate a significant material flux, likely from hydrothermal and volcanic origin. It is important to note that the recovery within the sediments of the volcanic signature identified at 1,000 m is not surprising, as this volcano is known for its recurrent eruptions since the eighteenth century (Ewart et al., 1977), in line with LSi_{XS} estimates at depths >3 cm below the seafloor (corresponding to the eighteenth century; see Table 1).

Station 5. The sediments at station 5 showed a medium Boström index, but lower than that estimated in the material collected at 1,000 m, possibly due to the additional distal impact of deeper sources (>1,500 m; Tilliette et al., 2022), feeding the sediments with high Fe_{XS}, Mn_{XS}, and Cu_{XS} (Figures 3 and 5c, Table 3). This distal hydrothermal origin was also supported by (a) the heterogeneous and large size of particles, much larger than clays (<3 μm; Horn et al., 1970; Leinen, 1989) and typical of distal transport (Feely et al., 1987, 1990; Lou et al., 2020; Ng et al., 2019), (b) the accumulation rates much higher than those of pelagic clays (x116-580; Li and Schoonmaker, 2003; Piper, 2005), and finally (c) the absence of Ni_{XS} and Zn_{XS} throughout the core (Figure 3), these elements being lost near sources. The presence of volcanic material (i.e., increasing the index value) is also strongly suspected in the sediments of this station, in view of the estimated continuous LSi_{XS} (sampled core dating from the nineteenth century to the present day according to accumulation rates, see Table 1) and the frequent eruptions of the Late'iki volcano since the eighteenth century (Ewart et al., 1977).

The very low Boström index of the sediments at Station 12 reflects a strong hydrothermal signature of a likely near-vent field with material exhibiting high Fe_{XS} and Mn_{XS} (Table 3, Figures 3 and 5c). Although this result was unexpected, the presence of a nearby source at the seafloor of station 12 is supported by the high accumulation rates (x122-610 relative to pelagic clays; Li and Schoonmaker, 2003), the particle size distribution, with grain up to 976 μm, typical of near-vent debris (Feely et al., 1987, 1990; Lou et al., 2020; Ng et al., 2019) as well as the high Zn_{XS}, Ni_{XS} and Cu_{XS}. Additional arguments in favor of the presence of strong hydrothermal activity in the vicinity of this station would be (a) the numerous reports of discolored waters and volcanic activity according to nautical charts of this area (SHOM C, 6817, INT605), (b) many potential active volcanic structures (>1,000 m; GEBCO Bathymetric Compilation Group, 2022), and (c) a mega-plume hypothesized within few kilometers of the station (20°28' S, 178°31' W), near the Lau Ridge (Guieu et al., 2018). It should be noted that no LSi_{EF} was estimated in these sediments, revealing that the large particle sizes estimated in this study originate solely from hydrothermal processes, consistent with the high Mn and low Al content.

4.3.2.2. In the South Pacific Gyre

Station 8 is located east of the Tonga Arc and was initially cored as a deep-sea detrital reference. However, the sediment index reveals a distal hydrothermal signature, as evidenced by high Fe_{XS}, Mn_{XS}, Cu_{XS} and, to a lesser extent, Pb_{XS} (Figures 3 and 5), although the estimated elemental excess were lower than in the Lau Basin. Consistent with these observations, the estimated sedimentation rates were 116–580 times higher than those of pelagic sediments (Li and Schoonmaker, 2003; Piper, 2005), indicating a great material flux. It is possible that this material originated from the east, for example, from the East Pacific Rise and/or other nearby deep hydrothermal source(s) (Kipp et al., 2018; Resing et al., 2015), although no DFe anomalies were detected in the deep waters at this station relative to DFe concentrations in water masses feeding the gyre region, albeit possibly due to the high threshold defined in that study (=0.2 nmol L^{-1}; Tilliette et al., 2022). This hypothesis is supported by the particle size falling within the range of hydrothermal particles involved in long-distance transport (1–50 μm; Feely et al., 1987, 1990; Lou et al., 2020). In addition, hydrothermal plumes have been reported to be transported thousands of kilometers away from their source at the ridge axis (Resing et al., 2015) and result in continuous fall-out of metals over large distances (Lilley et al., 2013), possibly up to station 8. Furthermore, Boström et al. (1969) also demonstrated the presence of sediments influenced by distal hydrothermalism near this site.

4.3.2.3. Detrital Component

As described in Section 4.3.1, microscopic inspection of particles collected in sediment traps at 1,000 m reveals the occurrence of a large abundance of basaltic glass, as evidenced by the sharp angle of large-sized particles. Escrig et al. (2012) collected fresh volcanic glass along the latitudinal location of the Fonualei Spreading Center (between −18° and −16°S) corresponding to an end-member of global back-arc lavas in the Lau Basin. These volcanic glasses exhibit average (Fe/Mn) ratio and Si content of 54 ± 5 and 25 ± 1 wt.%, respectively. Here, we were able to determine the geochemical composition of the detrital material based on geochemical

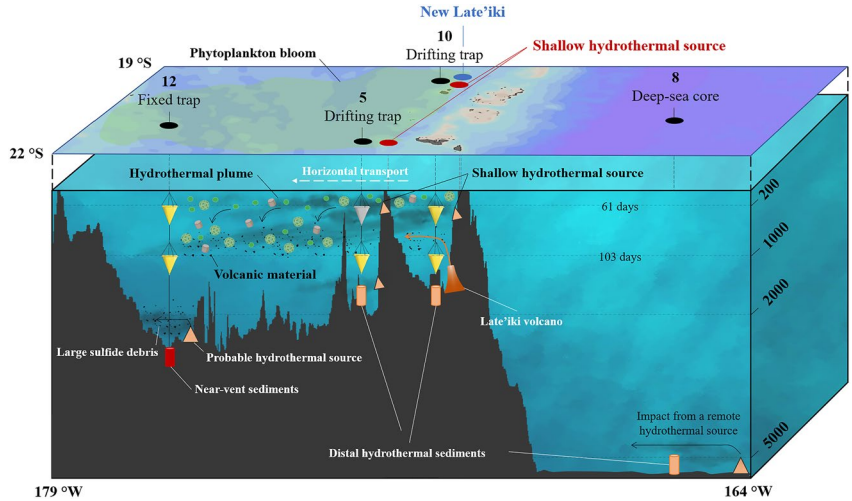

Figure 7. Summary diagram of the main results of the present study. These include (1) the non-vertical sinking of particles; (2) the impact of shallow hydrothermal plumes on all sediment traps in the Lau Basin; (3) the impact of volcanic material from the Late'iki volcano eruption on the deep traps deployed at stations 5, 10 and 12; (4) the impact of shallow and deep hydrothermalism, along with submarine volcanism, on seafloor sediments; (5) the impact of a distal hydrothermal source on the sediments at the deep-sea reference site; and (6) the impact of the potential deep hydrothermal source deduced near station 12. Note that no sample could be collected from the 200 m-trap deployed at station 5 (shaded) due to a PPS-5 malfunction. The days shown on the 200 and 1,000 m lines indicate the travel time of particles from the Tonga Arc to the fixed trap site at these depths.

features measured in the seafloor sediments. Following the calculations presented in Section 2.4.2, the average detrital fraction is characterized by $(Fe/Mn)_{det}$ and Si_{det} at 54 ± 3 and 22 ± 5 wt.%, respectively. These chemical signatures are extremely similar to those of the volcanic glasses analyzed by Escrig et al. (2012) as well as for trace metal such as Ni. Nevertheless, the detrital fraction is 10 and 2 times more enriched in Pb and Zn, respectively. This suggests that the hydrothermal contribution has been underestimated, as mentioned in Section 2.4.2, since hydrothermalism is the only explanation for such strong enrichments (Adams et al., 2006; Canion & Landsberger, 2013; Taylor, 1964). Overall, the detrital fraction identified, observed and analyzed here exhibits morphology and geochemical features that are consistent with a nearby volcanic origin solely.

5. Conclusion

In this study, deployment of sediment traps and coring of seafloor sediments allowed the identification and characterization of biogenic and hydrothermally-derived particles along the Tonga Arc over large spatio-temporal scales, from the Lau Ridge to the western border of the South Pacific gyre (along ~20°S; Figure 7). Consistent with the high biological productivity previously reported in the Lau Basin, large quantities of biogenic material (organic matter, opal and calcium carbonate) were collected at 200 and 1,000 m during the austral summer period. These particles were intimately related to the influx of lithogenic material from the Tonga Arc, whose hydrothermal origin could be resolved through numerous geochemical tracers (Al, Ca, Cu, Fe, Mn, Ni, Pb, Si, Zn). Such a result suggests that surface production is tightly linked to hydrothermal supply within the Lau Basin photic layer. Seafloor sediments from all stations also exhibited a metal-rich hydrothermal signature (Fe, Mn-rich, Al-depleted), supported by their high accumulation rates as well as the coarse and heterogeneous size of the sedimented particles, typical of hydrothermal oxide and/or sulfide debris. Thus, the sinking and sedimented particles were primarily from shallow to deep hydrothermal sources identified along the Tonga Arc. This set of evidence supports a major influence of hydrothermal sources and refutes the island effect often considered in this region.

Shallow and/or deep hydrothermal sources impacted the composition of sinking and sedimented particles at all stations sampled in the Lau Basin. The effect of the sources on the particle signature depended on their distance from the sampled site. The signature of hydrothermal material was pronounced in the sediment traps deployed at stations 5 and 10 (~15 km from the arc and identified shallow sources). It was also revealed but to a lesser extent at station 12, located near the Lau Ridge (~200 km from the arc), and was primarily reflected through Fe

enrichments in the water column both at the surface (200 m) and at depth (1,000 m). At all stations, besides the impact of hydrothermalism, a volcanic signature (Fe, LSi, Al-rich, Mn-depleted) was identified in the particles collected in the deepest sediment trap. This abundant volcanic material probably originated from the recent eruption of the Late'iki submarine volcano and the subsequent fast erosion of the newly created island, as confirmed through the observation of basaltic glass in the 1,000 m-trap at station 10. Surprisingly, the seafloor at station 12 reflects a deep hydrothermal activity, as evidenced by the typical signature of sulfide debris found near hydrothermal vents and the large and heterogeneous particle size. At the South Pacific gyre deep-sea reference site, the Al-Fe-Mn tracing in the seafloor sediments detected the distal impact of a deep hydrothermal source, likely present along the East Pacific Rise.

All these data lead to the conclusion that a myriad of shallow and deep hydrothermal sources, located along the Tonga Arc, fertilize the entire Lau Basin with numerous elements, including Fe, triggering significant POC production during the austral summer period, when the temperature conditions required for the diazotroph development are fulfilled. These hydrothermal sources, along with submarine volcanism, have a significant impact on the biogeochemistry of the Lau Basin, at very large spatial (from the Tonga Arc to the Lau Ridge) and temporal (from seasonal to centennial time scales in seafloor sediments) scales. This study also illustrates the importance of employing considerable care in interpreting sediment trap data, as these are certainly influenced by physical dynamics, thus greatly affecting the vertical sinking of collected particles.

Future research is needed to probe the seafloor near station 12 for acoustic and chemical anomalies to identify the hydrothermal source(s) responsible for the presence of large, metal-rich sedimented particles. Finally, molecular analyses could be interesting to characterize the different bacteria and/or archaea present in the water-sediment interface and to draw conclusions on the low $CaCO_3$ preservation observed in the seafloor sediments along the Tonga Arc.

Conflict of Interest

The authors declare no conflicts of interest relevant to this study.

Data Availability Statement

The data used in this study are publicly available on the SEANOE database (Guieu et al., 2022) (http://doi.org/10.17882/88169).

Acknowledgments

This work was carried out in the framework of the TONGA project (TONGA cruise GEOTRACES GPpr14 November 2019, https://doi.org/10.17600/18000884) managed by the LOV (CG) and the MIO. The project was funded by the TGIR Flotte Océanographique Française, the A-MIDeX of Aix-Marseille University, the LEFE-CYBER and GMMC program and the Agence Nationale de Recherche (ANR-18-CE01-0016). We warmly thank all the scientists, the captain and the crew of the R/V L'Atalante for their cooperative work at sea. We thank the crew of the R/V Alis (TGIR Flotte, operated by IFREMER) for the safe recovery of the fixed mooring in particularly difficult weather conditions. We thank Faustine Fauche for her help in the analysis of trap and core samples. We thank the SNAPO-CO_2 platform for carbonate chemistry analyzes. We thank Christophe Maes and Nicolas Grima for their help in positioning the fixed mooring line and for the Lagrangian analyses. We thank Cédric Boulart and Jean-Philippe Gac for their help with sediment sampling.

References

Adams, A., Christiansen, E., Kowallis, B., Carranza-Castañeda, O., & Miller, W. (2006). Contrasting silicic Magma series in Miocene-Pliocene ash deposits in the san Miguel de Allende Graben, Guanajuato, Mexico. *The Journal of Geology*, *114*(2), 247–266. https://doi.org/10.1086/499633

Almirón, J., Vargas, M., Tupayachy-Quispe, D., Duquesne, S., Roudet, F., & Silva-Vela, A. (2021). Influence of the process of synthesis of zeolites from volcanic ash in its synergistic action as a flame-retardant for polypropylene composites. *Buildings*, *12*(1), 24. https://doi.org/10.3390/buildings12010024

Anderson, M. O., Norris-Julseth, C., Rubin, K. H., Haase, K., Hannington, M. D., Baxter, A. T., & Stewart, M. S. (2021). Geologic and structural evolution of the NE Lau Basin, Tonga: Morphotectonic analysis and classification of structures using shallow seismicity. *Frontiers in Earth Science*, *9*, 665185. https://doi.org/10.3389/feart.2021.665185

Bailey, D. K. (1993). Carbonate magmas. *JGS*, *150*(4), 637–651. https://doi.org/10.1144/gsjgs.150.4.0637

Baker, C. A., Estapa, M. L., Iversen, M., Lampitt, R., & Buesseler, K. (2020). Are all sediment traps created equal? An intercomparison study of carbon export methodologies at the PAP-SO site. *Progress in Oceanography*, *184*, 102317. https://doi.org/10.1016/j.pocean.2020.102317

Baker, E. T., Walker, S. L., Massoth, G. J., & Resing, J. A. (2019). The NE Lau Basin: Widespread and abundant hydrothermal venting in the back-arc region behind a superfast subduction zone. *Frontiers in Marine Science*, *6*, 382. https://doi.org/10.3389/fmars.2019.00382

Barrett, T. J., Jarvis, I., Hannington, M. D., & Thirlwall, M. F. (2021). Chemical characteristics of modern deep-sea metalliferous sediments in closed versus open basins, with emphasis on rare-earth elements and Nd isotopes. *Earth-Science Reviews*, *222*, 103801. https://doi.org/10.1016/j.earscirev.2021.103801

Beaulieu, S. E., & Szafrański, K. M. (2020). InterRidge global database of active submarine hydrothermal vent fields. Version 3 (4). *PANGAEA*. https://doi.org/10.1594/PANGAEA.917894

Berger, W. H., Smetacek, V., & Wefer, G. (1989). Ocean productivity and paleoproductivity - An overview. In *Productivity of the oceans present and past* (pp. 1–34). Wiley.

Bodungen, B. V., Wunsch, M., & Fürderer, H. (2013). Sampling and analysis of suspended and sinking particles in the northern North Atlantic. In D. C. Hurd & D. W. Spencer (Eds.), *Geophysical monograph series* (pp. 47–56). American Geophysical Union. https://doi.org/10.1029/GM063p0047

Bonnet, S., Caffin, M., Berthelot, H., & Moutin, T. (2017). Hot spot of N_2 fixation in the western tropical South Pacific pleads for a spatial decoupling between N_2 fixation and denitrification. *Proceedings of the National Academy of Sciences of the United States of America*, *114*(14), E2800–E2801. https://doi.org/10.1073/pnas.1619514114

Bonnet, S., Guieu, C., Taillandier, V., Boulart, C., Bouruet-Aubertot, P., Gazeau, F., et al. (2023). Natural iron fertilization by shallow hydrothermal sources fuels diazotroph blooms in the ocean. *Science*, *380*(6647), 812–817. https://doi.org/10.1126/science.abq4654

Boström, K., & Peterson, M. N. A. (1969). The origin of aluminum-poor ferromanganoan sediments in areas of high heat flow on the East Pacific Rise. *Marine Geology*, *7*(5), 427–447. https://doi.org/10.1016/0025-3227(69)90016-4

Boström, K., Peterson, M. N. A., Joensuu, O., & Fisher, D. E. (1969). Aluminum-poor ferromanganoan sediments on active oceanic ridges. *Journal of Geophysical Research*, *74*(12), 3261–3270. https://doi.org/10.1029/JB074i012p03261

Boyd, P. W., & Trull, T. W. (2007). Understanding the export of biogenic particles in oceanic waters: Is there consensus? *Progress in Oceanography*, *72*(4), 276–312. https://doi.org/10.1016/j.pocean.2006.10.007

Brzezinski, M. A., & Nelson, D. M. (1995). The annual silica cycle in the Sargasso Sea near Bermuda. *Deep Sea Research Part I: Oceanographic Research Papers*, *42*(7), 1215–1237. https://doi.org/10.1016/0967-0637(95)93592-3

Buesseler, K. O., Antia, A. N., Chen, M., Fowler, S. W., Gardner, W. D., Gustafsson, O., et al. (2007). An assessment of the use of sediment traps for estimating upper ocean particle fluxes. *Journal of Marine Research*, *65*(3), 345–416. https://doi.org/10.1357/002224007781567621

Butman, C. A. (1986). Sediment trap biases in turbulent flows: Results from a laboratory flume study. *Journal of Marine Research*, *44*(3), 645–693. https://doi.org/10.1357/002224086788403051

Canion, B., & Landsberger, S. (2013). Trace analysis and leaching dynamics of volcanic ash using NAA and ICP-MS. *Journal of Radioanalytical and Nuclear Chemistry*, *296*(1), 375–378. https://doi.org/10.1007/s10967-012-2069-3

Carpenter, E. J., & Capone, D. G. (1992). Nitrogen fixation in Trichodesmium blooms. In E. J. Carpenter, D. G. Capone, & J. G. Rueter (Eds.), *Marine pelagic cyanobacteria: Trichodesmium and other diazotrophs, NATO ASI Series* (pp. 211–217). Springer Netherlands. https://doi.org/10.1007/978-94-015-7977-3_13

Cave, R. (2002). *A geochemical study of hydrothermal signals in marine sediments: The rainbow hydro thermal area, 36 degrees on the mid-Atlantic ridge (PhD Thesis)*. University of Southampton.

Cave, R. R., German, C. R., Thomson, J., & Nesbitt, R. W. (2002). Fluxes to sediments underlying the Rainbow hydrothermal plume at 36°14′N on the Mid-Atlantic Ridge. *Geochimica et Cosmochimica Acta*, *66*(11), 1905–1923. https://doi.org/10.1016/S0016-7037(02)00823-2

Chavagnac, V., German, C. R., Milton, J. A., & Palmer, M. R. (2005). Sources of REE in sediment cores from the Rainbow vent site (36°14′N, MAR). *Chemical Geology*, *216*(3–4), 329–352. https://doi.org/10.1016/j.chemgeo.2004.11.015

Chavagnac, V., German, C. R., & Taylor, R. N. (2008). Global environmental effects of large volcanic eruptions on ocean chemistry: Evidence from "hydrothermal" sediments (ODP Leg 185, Site 1149B). *Journal of Geophysical Research*, *113*(B6), B06201. https://doi.org/10.1029/2007JB005333

Cronan, D. S. (1972). The Mid-Atlantic ridge near 45°N, XVII: Al, as, Hg, and Mn in Ferruginous sediments from the median valley. *Canadian Journal of Earth Sciences*, *9*(3), 319–323. https://doi.org/10.1139/e72-025

Deuser, W. G. (1987). Seasonal variations in isotopic composition and deep-water fluxes of the tests of perennially abundant planktonic foraminifera of the Sargasso Sea; results from sediment-trap collections and their paleoceanographic significance. *Journal of Foraminiferal Research*, *17*(1), 14–27. https://doi.org/10.2113/gsjfr.17.1.14

Deuser, W. G., & Ross, E. H. (1980). Seasonal change in the flux of organic carbon to the deep Sargasso Sea. *Nature*, *283*(5745), 364–365. https://doi.org/10.1038/283364a0

Dick, G. J., Anantharaman, K., Baker, B. J., Li, M., Reed, D. C., & Sheik, C. S. (2013). The microbiology of deep-sea hydrothermal vent plumes: Ecological and biogeographic linkages to seafloor and water column habitats. *Frontiers in Microbiology*, *4*. https://doi.org/10.3389/fmicb.2013.00124

Ducklow, H., Steinberg, D., & Buesseler, K. (2001). Upper Ocean carbon export and the biological pump. *Oceanography*, *14*(4), 50–58. https://doi.org/10.5670/oceanog.2001.06

Dutkiewicz, A., Müller, R. D., Hogg, A. M. C., & Spence, P. (2016). Vigorous deep-sea currents cause global anomaly in sediment accumulation in the Southern Ocean. *Geology*, *44*(8), 663–666. https://doi.org/10.1130/G38143.1

Dymond, J. (1981). Geochemistry of Nazca plate surface sediments: An evaluation of hydrothermal, biogenic, detrital, and hydrogenous sources. In *Geological Society of America Memoirs* (pp. 133–174). Geological Society of America. https://doi.org/10.1130/MEM154-p133

Edmonds, H. N., & German, C. R. (2004). Particle geochemistry in the rainbow hydrothermal plume, Mid-Atlantic ridge. *Geochimica et Cosmochimica Acta*, *68*(4), 759–772. https://doi.org/10.1016/S0016-7037(03)00498-8

Emerson, S., & Hedges, J. I. (1988). Processes controlling the organic carbon content of open ocean sediments. *Paleoceanography*, *3*(5), 621–634. https://doi.org/10.1029/PA003i005p00621

Escrig, S., Bézos, A., Langmuir, C. H., Michael, P. J., & Arculus, R. (2012). Characterizing the effect of mantle source, subduction input and melting in the Fonualei Spreading center, Lau Basin: Constraints on the origin of the boninitic signature of the back-arc lavas: Geochemical variation along the FSC. *Geochemistry, Geophysics, Geosystems*, *13*(10). https://doi.org/10.1029/2012gc004130

Ewart, A., Brothers, R. N., & Mateen, A. (1977). An outline of the geology and geochemistry, and the possible petrogenetic evolution of the volcanic rocks of the Tonga-Kermadec-New Zealand island arc. *Journal of Volcanology and Geothermal Research*, *2*(3), 205–250. https://doi.org/10.1016/0377-0273(77)90001-4

Feely, R. A., Geiselman, T. L., Baker, E. T., Massoth, G. J., & Hammond, S. R. (1990). Distribution and composition of hydrothermal plume particles from the ASHES vent field at axial volcano, juan de Fuca ridge. *Journal of Geophysical Research*, *95*(B8), 12855–12873. https://doi.org/10.1029/JB095iB08p12855

Feely, R. A., Lewison, M., Massoth, G. J., Robert-Baldo, G., Lavelle, J. W., Byrne, R. H., et al. (1987). Composition and dissolution of black smoker particulates from active vents on the Juan de Fuca Ridge. *Journal of Geophysical Research*, *92*(B11), 11347–11363. https://doi.org/10.1029/JB092iB11p11347

Fiantis, D., Nelson, M., Shamshuddin, J., Goh, T. B., & Van Ranst, E. (2010). Determination of the geochemical weathering indices and trace elements content of new volcanic ash deposits from Mt. Talang (West Sumatra) Indonesia. *Eurasian Soil Science*, *43*(13), 1477–1485. https://doi.org/10.1134/S1064229310130077

Gardner, W. (1980). Field calibration of sediment traps. *Journal of Marine Research*, *30*, 311–323.

GEBCO Bathymetric Compilation Group. (2022). The GEBCO_2022 Grid - A continuous terrain model of the global oceans and land. https://doi.org/10.5285/E0F0BB80-AB44-2739-E053-6C86ABC0289C

German, C. R., Bourlés, D. L., Brown, E. T., Hergt, J., Colley, S., Higgs, N. C., et al. (1997). Hydrothermal scavenging on the juan de Fuca ridge: 23OThxs, 10Be, and REEs in ridge-flank sediments. *Geochimica et Cosmochimica Acta*, *61*(19), 4067–4078. https://doi.org/10.1016/S0016-7037(97)00230-5

Gersonde, R., Crosta, X., Abelmann, A., & Armand, L. (2005). Sea-Surface temperature and sea ice distribution of the southern ocean at the EPILOG Last Glacial maximum—A circum-Antarctic view based on siliceous microfossil records. *Quaternary Science Reviews*, *24*(7–9), 869–896. https://doi.org/10.1016/j.quascirev.2004.07.015

González-Vega, A., Fraile-Nuez, E., Santana-Casiano, J. M., González-Dávila, M., Escánez-Pérez, J., Gómez-Ballesteros, M., et al. (2020). Significant release of dissolved inorganic nutrients from the shallow submarine volcano Tagoro (canary islands) based on seven-year monitoring. *Frontiers in Marine Science*, *6*, 829. https://doi.org/10.3389/fmars.2019.00829

Guieu, C. (2020). *Tonga RECUP cruise*. Alis R/V. https://doi.org/10.17600/18001357

Guieu, C., & Bonnet, S. (2019). *Tonga cruise 2019*. L'Atalante R/V. https://doi.org/10.17600/18000884

Guieu, C., Bonnet, S., Abadou, F., Alliouane, S., Arnaud-Haond, S., Arnone, V., et al. (2022). Biogeochemical dataset collected during the Tonga cruise. https://doi.org/10.17882/88169

Guieu, C., Bonnet, S., Petrenko, A., Menkes, C., Chavagnac, V., Desboeufs, K., et al. (2018). Iron from a submarine source impacts the productive layer of the Western Tropical South Pacific (WTSP). *Scientific Reports*, *8*, 1–9. https://doi.org/10.1038/s41598-018-27407-z

Guieu, C., Roy-Barman, M., Leblond, N., Jeandel, C., Souhaut, M., Le Cann, B., et al. (2005). Vertical particle flux in the northeast Atlantic Ocean (POMME experiment). *Journal of Geophysical Research*, *110*(C7). https://doi.org/10.1029/2004JC002672

Hargrave, B. T., & Burns, N. M. (1979). Assessment of sediment trap collection efficiency. *Limnology & Oceanography*, *24*(6), 1124–1136. https://doi.org/10.4319/lo.1979.24.6.1124

Ho, T.-Y., Quigg, A., Finkel, Z. V., Milligan, A. J., Wyman, K., Falkowski, P. G., & Morel, F. M. M. (2003). The elemental composition of some marine phytoplankton. *Journal of Phycology*, *39*(6), 1145–1159. https://doi.org/10.1111/j.0022-3646.2003.03-090.x

Honjo, S., Spencer, D. W., & Gardner, W. D. (1992). A sediment trap intercomparison experiment in the Panama Basin, 1979. Deep Sea Research Part A. *Oceanographic Research Papers*, *39*(2), 333–358. https://doi.org/10.1016/0198-0149(92)90112-7

Horn, D. R., Horn, B. M., & Delach, M. N. (1970). *Sedimentary provinces of the North Pacific* (pp. 1–22). Geological Society of America Memoirs. https://doi.org/10.1130/MEM126-p1

Humphris, S. E., Herzig, P. M., Miller, D. J., Alt, J. C., Becker, K., Brown, D., et al. (1995). The internal structure of an active sea-floor massive sulphide deposit. *Nature*, *377*(6551), 713–716. https://doi.org/10.1038/377713a0

Hüneke, H., & Henrich, R. (2011). Pelagic sedimentation in modern and Ancient oceans. In *Developments in sedimentology* (pp. 215–351). Elsevier. https://doi.org/10.1016/B978-0-444-53000-4.00004-4

Hurd, D. C. (1972). Factors affecting solution rate of biogenic opal in seawater. *Earth and Planetary Science Letters*, *15*(4), 411–417. https://doi.org/10.1016/0012-821X(72)90040-4

Imai, N., Terashima, S., Itoh, S., & Ando, A. (1995). 1994 Compilation of analytical data for minor and trace elements in seventeen GSJ geochemical reference samples, "igneous rock series.". *Geostandards and Geoanalytical Research*, *19*(2), 135–213. https://doi.org/10.1111/j.1751-908X.1995.tb00158.x

Johnson, K. S., Gordon, R. M., & Coale, K. H. (1997). What controls dissolved iron concentrations in the world ocean? *Marine Chemistry*, *57*(3–4), 137–161. https://doi.org/10.1016/S0304-4203(97)00043-1

Karl, D. M. (1995). *The microbiology of deep-sea hydrothermal vents*. CRC-Press.

Kipp, L. E., Sanial, V., Henderson, P. B., Van Beek, P., Reyss, J.-L., Hammond, D. E., et al. (2018). Radium isotopes as tracers of hydrothermal inputs and neutrally buoyant plume dynamics in the deep ocean. *Marine Chemistry*, *201*, 51–65. https://doi.org/10.1016/j.marchem.2017.06.011

Klaas, C., & Archer, D. E. (2002). Association of sinking organic matter with various types of mineral ballast in the deep sea: Implications for the rain ratio. *Global Biogeochemical Cycles*, *16*(4), 63-1–63-14. https://doi.org/10.1029/2001GB001765

Kyte, F. T., Leinen, M., Ross Heath, G., & Zhou, L. (1993). Cenozoic sedimentation history of the central North Pacific: Inferences from the elemental geochemistry of core LL44-GPC3. *Geochimica et Cosmochimica Acta*, *57*(8), 1719–1740. https://doi.org/10.1016/0016-7037(93)90109-A

Leinen, M. (1989). The pelagic clay province of the North Pacific Ocean. In E. L. Winterer, D. M. Hussong, & R. W. Decker (Eds.), *The eastern Pacific Ocean and Hawaii* (pp. 323–335). Geological Society of America. https://doi.org/10.1130/DNAG-GNA-N.323

Leonelli, C., Kamseu, E., Boccaccini, D. N., Melo, U. C., Rizzuti, A., Billong, N., & Miselli, P. (2007). Volcanic ash as alternative raw materials for traditional vitrified ceramic products. *Advances in Applied Ceramics*, *106*(3), 135–141. https://doi.org/10.1179/174367607X159329

Li, Y.-H., & Schoonmaker, J. E. (2003). Chemical composition and mineralogy of marine sediments. In *Treatise on geochemistry* (pp. 1–35). Elsevier. https://doi.org/10.1016/B0-08-043751-6/07088-2

Lilley, M. D., Feely, R. A., & Trefry, J. H. (2013). Chemical and biochemical transformations in hydrothermal plumes. In *Seafloor hydrothermal systems: Physical, chemical, biological, and geological interactions* (pp. 369–391). American Geophysical Union (AGU). https://doi.org/10.1029/GM091p0369

Locarnini, R., Mishonov, A., Baranova, O., Boyer, T., Zweng, M., Garcia, H., et al. (2018). *World Ocean Atlas 2018, Volume 1: Temperature* (Vol. 81, p. 52). NOAA Atlas NESDIS.

Lou, Y., He, Z., & Han, X. (2020). Transport and deposition patterns of particles Laden by Rising submarine hydrothermal plumes. *Geophysical Research Letters*, *47*(20). https://doi.org/10.1029/2020GL089935

Lupton, J. E., Pyle, D. G., Jenkins, W. J., Greene, R., & Evans, L. (2004). Evidence for an extensive hydrothermal plume in the Tonga-Fiji region of the South Pacific. *Geochemistry, Geophysics, Geosystems*, *5*(1). https://doi.org/10.1029/2003GC000607

Mahiques, M. M., Sousa, S. H. M., Burone, L., Nagai, R. H., Silveira, I. C. A., Figueira, R. C. L., et al. (2011). Radiocarbon geochronology of the sediments of the São Paulo Bight (southern Brazilian upper margin). *Anais da Academia. Brasileira de Ciências*, *83*(3), 817–834. https://doi.org/10.1590/S0001-37652011005000028

Massoth, G., Baker, E., Worthington, T., Lupton, J., De Ronde, C., Arculus, R., et al. (2007). Multiple hydrothermal sources along the south Tonga arc and Valu Fa Ridge. *Geochemistry, Geophysics, Geosystems*, *8*(11). https://doi.org/10.1029/2007GC001675

Massoth, G. J., Baker, E. T., Feely, R. A., Lupton, J. E., Collier, R. W., Gendron, J. F., et al. (1998). Manganese and iron in hydrothermal plumes resulting from the 1996 Gorda Ridge Event. *Deep Sea Research Part II: Topical Studies in Oceanography*, *45*(12), 2683–2712. https://doi.org/10.1016/S0967-0645(98)00089-7

McCave, I. N. (1975). Vertical flux of particles in the ocean. *Deep Sea Research and Oceanographic Abstracts*, *22*(7), 491–502. https://doi.org/10.1016/0011-7471(75)90022-4

Mills, R., Elderfield, H., & Thomson, J. (1993). A dual origin for the hydrothermal component in a metalliferous sediment core from the Mid-Atlantic Ridge. *Journal of Geophysical Research*, *98*(B6), 9671–9681. https://doi.org/10.1029/92JB01414

Mills, R. A., & Elderfield, H. (1995). Hydrothermal activity and the geochemistry of metalliferous sediment. In S. E. Humphris, R. A. Zierenberg, L. S. Mullineaux, & R. E. Thomson (Eds.), *Geophysical monograph series* (pp. 392–407). American Geophysical Union. https://doi.org/10.1029/GM091p0392

Morse, J. W., Arvidson, R. S., & Lüttge, A. (2007). Calcium carbonate formation and dissolution. *Chemical Reviews*, *107*(2), 342–381. https://doi.org/10.1021/cr050358j

Mortlock, R. A., & Froelich, P. N. (1989). A simple method for the rapid determination of biogenic opal in pelagic marine sediments. Deep Sea Research Part A. *Oceanographic Research Papers*, *36*(9), 1415–1426. https://doi.org/10.1016/0198-0149(89)90092-7

Mosseri, J., Quéguiner, B., Rimmelin, P., Leblond, N., & Guieu, C. (2005). Silica fluxes in the northeast Atlantic frontal zone of Mode Water formation (38°–45°N, 16°–22°W) in 2001–2002. *Journal of Geophysical Research*, *110*(C7), C07S19. https://doi.org/10.1029/2004JC002615

Naji, J. A., & Asi, I. M. (2008). Performance evaluation of asphalt concrete mixes containing granular volcanic ash. *Journal of Materials in Civil Engineering*, *20*, 754–761. https://doi.org/10.1061/(asce)0899-1561(2008)20:12(754)

Nelson, D. M., & Brzezinski, M. A. (1997). Diatom growth and productivity in an oligo-trophic midocean gyre: A 3-yr record from the Sargasso sea near Bermuda. *Limnology & Oceanography*, *42*(3), 473–486. https://doi.org/10.4319/lo.1997.42.3.0473

Nelson, D. M., Smith, W. O., Muench, R. D., Gordon, L. I., Sullivan, C. W., & Husby, D. M. (1989). Particulate matter and nutrient distributions in the ice-edge zone of the Weddell sea: Relationship to hydrography during late summer. *Deep-Sea Research, Part A: Oceanographic Research Papers*, *36*(2), 191–209. https://doi.org/10.1016/0198-0149(89)90133-7

Nelson, D. M., Tréguer, P., Brzezinski, M. A., Leynaert, A., & Quéguiner, B. (1995). Production and dissolution of biogenic silica in the ocean: Revised global estimates, comparison with regional data and relationship to biogenic sedimentation. *Global Biogeochemical Cycles*, *9*(3), 359–372. https://doi.org/10.1029/95GB01070

Ng, W.-L., Chen, C.-A., Kawi, S. D., Musta, B., & Chan, T.-Y. (2019). Effects of hydrogen peroxide treatment on the particle size distribution of hydrothermal vent sediments: A case study in Guishan island, Taiwan. *Borneo Journal of Marine Science and Aquaculture (BJoMSA)*, *3*(2), 52–56. https://doi.org/10.51200/bjomsa.v3i2.1995

Nohara, M., & Yokoto, S. (1978). The geochemistry of trace elements in pelagic sediments from the central Pacific basin. *The Journal of the Geological Society of Japan*, *84*(4), 165–175. https://doi.org/10.5575/geosoc.84.165

Oskarasson, N. (2010). Chemical analysis of rocks from the Eyjafjallajökull 2010 eruptions.

Pelletier, B., Calmant, S., & Pillet, R. (1998). Current tectonics of the Tonga–new Hebrides region. *Earth and Planetary Science Letters*, *164*(1–2), 263–276. https://doi.org/10.1016/S0012-821X(98)00212-X

Piper, D. J. W. (2005). Sedimentary processes | deep water processes and deposits. In *Encyclopedia of geology* (pp. 641–649). Elsevier. https://doi.org/10.1016/B0-12-369396-9/00496-2

Plank, S., Marchese, F., Genzano, N., Nolde, M., & Martinis, S. (2020). The short life of the volcanic island New Late'iki (Tonga) analyzed by multi-sensor remote sensing data. *Scientific Reports*, *10*(1), 22293. https://doi.org/10.1038/s41598-020-79261-7

Plank, T., Kelley, K. A., Murray, R. W., & Stern, L. Q. (2007). Chemical composition of sediments subducting at the Izu-Bonin trench: Chemical composition of sediments. *Geochemistry, Geophysics, Geosystems*, *8*(4). https://doi.org/10.1029/2006gc001444

Raven, J. A. (1988). The iron and molybdenum use efficiencies of plant growth with different energy, carbon and nitrogen sources. *New Phytologist*, *109*(3), 279–287. https://doi.org/10.1111/j.1469-8137.1988.tb04196.x

Razzhigaeva, N. G., Ganzei, L. A., Grebennikova, T. A., Mokhova, L. M., Kopoteva, T. A., Rybin, A. V., & Kharlamov, A. A. (2009). The peat bog of Ketoi island: The middle-upper holocene reference section of the central Kuriles. *Russian Journal of Pacific Geology*, *3*(6), 570–584. https://doi.org/10.1134/S1819714009060050

Redfield, A. C., Ketchum, B. H., & Richards, F. A. (1963). The influence of organisms on the composition of sea-water. In *The composition of seawater: Comparative and descriptive oceanography, the sea* (pp. 26–77). Interscience Publishers.

Resing, J. A., & Sansone, F. J. (1999). The chemistry of lava–seawater interactions: The generation of acidity. *Geochimica et Cosmochimica Acta*, *63*(15), 2183–2198. https://doi.org/10.1016/S0016-7037(99)00193-3

Resing, J. A., Sedwick, P. N., German, C. R., Jenkins, W. J., Moffett, J. W., Sohst, B. M., & Tagliabue, A. (2015). Basin-scale transport of hydrothermal dissolved metals across the South Pacific Ocean. *Nature*, *523*(7559), 200–203. https://doi.org/10.1038/nature14577

Robbins, J. A., & Edgington, D. N. (1975). Determination of recent sedimentation rates in Lake Michigan using Pb-210 and Cs-137. *Geochimica et Cosmochimica Acta*, *39*(3), 285–304. https://doi.org/10.1016/0016-7037(75)90198-2

Rousselet, L., De Verneil, A., Doglioli, A. M., Petrenko, A. A., Duhamel, S., Maes, C., & Blanke, B. (2018). Large-to submesoscale surface circulation and its implications on biogeochemical/biological horizontal distributions during the OUTPACE cruise (southwest Pacific). *Biogeosciences*, *15*(8), 2411–2431. https://doi.org/10.5194/bg-15-2411-2018

Sakaguchi, A., Kimura, G., Strasser, M., Screaton, E. J., Curewitz, D., & Murayama, M. (2011). Episodic seafloor mud brecciation due to great subduction zone earthquakes. *Geology*, *39*(10), 919–922. https://doi.org/10.1130/G32043.1

Sarmiento, J. L., & Gruber, N. (2006). *Ocean biogeochemical dynamics*. Princeton University Press.

Sayles, F. L., & Bischoff, J. L. (1973). Ferromanganoan sediments in the equatorial East Pacific. *Earth and Planetary Science Letters*, *19*(3), 330–336. https://doi.org/10.1016/0012-821X(73)90083-6

Schmidt, S., Howa, H., Diallo, A., Martín, J., Cremer, M., Duros, P., et al. (2014). Recent sediment transport and deposition in the Cap-Ferret Canyon, south-east margin of Bay of Biscay. *Deep Sea Research Part II: Topical Studies in Oceanography*, *104*, 134–144. https://doi.org/10.1016/j.dsr2.2013.06.004

Stoffers, P., Worthington, T. J., Schwarz-Schampera, U., Hannington, M. D., Massoth, G. J., Hekinian, R., et al. (2006). Submarine volcanoes and high-temperature hydrothermal venting on the Tonga arc, southwest Pacific. *Geology*, *34*(6), 453. https://doi.org/10.1130/G22227.1

Taylor, S. R. (1964). Abundance of chemical elements in the continental crust: A new table. *Geochimica et Cosmochimica Acta*, *28*(8), 1273–1285. https://doi.org/10.1016/0016-7037(64)90129-2

Taylor, S. R., & McLennan, S. M. (1985). *The continental crust: Its composition and evolution: An examination of the geochem. Record preserved in sedimentary rocks, geoscience texts*. Blackwell.

Tchakoute Kouamo, H., Elimbi, A., Mbey, J. A., Ngally Sabouang, C. J., & Njopwouo, D. (2012). The effect of adding alumina-oxide to metakaolin and volcanic ash on geopolymer products: A comparative study. *Construction and Building Materials*, *35*, 960–969. https://doi.org/10.1016/j.conbuildmat.2012.04.023

Tilliette, C., Gazeau, F., Portlock, G., Benavides, M., Bonnet, S., Guigue, C., et al. (2023). Influence of shallow hydrothermal fluid release on the functioning of phytoplankton communities. *Frontiers in Marine Science*, *10*, 1082077. https://doi.org/10.3389/fmars.2023.1082077

Tilliette, C., Taillandier, V., Bouruet-Aubertot, P., Grima, N., Maes, C., Montanes, M., et al. (2022). Dissolved iron patterns impacted by shallow hydrothermal sources along a transect through the Tonga-Kermadec arc. *Global Biogeochemical Cycles*, *36*(7). https://doi.org/10.1029/2022GB007363

Timm, C., Bassett, D., Graham, I. J., Leybourne, M. I., De Ronde, C. E. J., Woodhead, J., et al. (2013). Louisville seamount subduction and its implication on mantle flow beneath the central Tonga–Kermadec arc. *Nature Communications*, *4*(1), 1720. https://doi.org/10.1038/ncomms2702

Tréguer, P., Nelson, D. M., Van Bennekom, A. J., DeMaster, D. J., Leynaert, A., & Quéguiner, B. (1995). The silica balance in the World Ocean: A Reestimate. *Science*, *268*(5209), 375–379. https://doi.org/10.1126/science.268.5209.375

Trocine, R. P., & Trefry, J. H. (1988). Distribution and chemistry of suspended particles from an active hydrothermal vent site on the Mid-Atlantic Ridge at 26°N. *Earth and Planetary Science Letters*, *88*(1–2), 1–15. https://doi.org/10.1016/0012-821X(88)90041-6

Turner, J. (2002). Zooplankton fecal pellets, marine snow and sinking phytoplankton blooms. *Aquatic Microbial Ecology*, *27*, 57–102. https://doi.org/10.3354/ame027057

Verardo, D. J., Froelich, P. N., & McIntyre, A. (1990). Determination of organic carbon and nitrogen in marine sediments using the Carlo Erba NA-1500 analyzer. Deep Sea Research Part A. *Oceanographic Research Papers*, *37*(1), 157–165. https://doi.org/10.1016/0198-0149(90)90034-S

Volk, T., & Hoffert, M. I. (2013). Ocean carbon pumps: Analysis of relative strengths and efficiencies in Ocean-driven atmospheric CO_2 changes. In E. T. Sundquist & W. S. Broecker (Eds.), *Geophysical monograph series* (pp. 99–110). American Geophysical Union. https://doi.org/10.1029/GM032p0099

Von Damm, K. L. (1990). Seafloor hydrothermal activity: Black smoker chemistry and chimneys. *Annual Review of Earth and Planetary Sciences*, *18*(1), 173–204. https://doi.org/10.1146/annurev.ea.18.050190.001133

Wefer, G., & Fischer, G. (1993). Seasonal patterns of vertical particle flux in equatorial and coastal upwelling areas of the eastern Atlantic. *Deep Sea Research Part I: Oceanographic Research Papers*, *40*(8), 1613–1645. https://doi.org/10.1016/0967-0637(93)90019-Y

Whiteside, A., Dupouy, C., Singh, A., Bani, P., Tan, J., & Frouin, R. (2023). Impact of ashes from the 2022 Tonga volcanic eruption on satellite ocean color signatures. *Frontiers in Marine Science*, *9*, 1028022. https://doi.org/10.3389/fmars.2022.1028022

Whiteside, A., Dupouy, C., Singh, A., Frouin, R., Menkes, C., & Lefèvre, J. (2021). Automatic detection of optical signatures within and around floating Tonga-Fiji Pumice Rafts using MODIS, VIIRS, and OLCI satellite sensors. *Remote Sensing*, *13*(3), 501. https://doi.org/10.3390/rs13030501

Zhang, H., Che, H., Xia, J., Cheng, Q., Qi, D., Cao, J., & Luo, Y. (2022). Sedimentary $CaCO_3$ accumulation in the deep west Pacific Ocean. *Frontiers in Earth Science*, *10*, 857260. https://doi.org/10.3389/feart.2022.857260

Zhang, Q., Snow, J. T., Holdship, P., Price, D., Watson, P., & Rickaby, R. E. M. (2018). Direct measurement of multi-elements in high matrix samples with a flow injection ICP-MS: Application to the extended *Emiliania huxleyi* Redfield ratio. *Journal of Analytical Atomic Spectrometry*, *33*(7), 1196–1208. https://doi.org/10.1039/C8JA00031J

Zierenberg, R. A., Adams, M. W. W., & Arp, A. J. (2000). Life in extreme environments: Hydrothermal vents. *Proceedings of the National Academy of Sciences*, *97*(24), 12961–12962. https://doi.org/10.1073/pnas.210395997

Ziveri, P., Rutten, A., De Lange, G. J., Thomson, J., & Corselli, C. (2000). Present-day coccolith fluxes recorded in central eastern Mediterranean sediment traps and surface sediments. *Palaeogeography, Palaeoclimatology, Palaeoecology*, *158*(3–4), 175–195. https://doi.org/10.1016/S0031-0182(00)00049-3